Optimized chemogenetic ablation and regeneration of enteric nervous system neurons in zebrafish

Mujahid Ali Shah[1], Katherine K. Moran[1], Helen Rueckert[1,2], Abigail V. Sharrock[3], David F. Ackerley[3], Jeff S. Mumm[4], Julia Ganz[1] *

[1]Department of Integrative Biology, Michigan State University, East Lansing, MI, USA, [2]Department of Cell Biology, Developmental and Stem Cell Biology Program, Duke University School of Medicine, Durham, NC, USA, [3]School of Biological Sciences, Victoria University of Wellington, Wellington, New Zealand, [4] Department of Ophthalmology, Wilmer Eye Institute, Johns Hopkins University, Baltimore, MD, USA.

***Correspondence**, ganz@msu.edu

Abstract

The enteric nervous system (ENS) is the intrinsic nervous system of the gut and regulates essential gut functions, including motility, digestion, and immune response, ensuring gut homeostasis. ENS dysfunction or loss is associated with gastrointestinal disorders such as Hirschsprung disease (HSCR). Currently, surgery is the only treatment for HSCR, but it often has lifelong, severe complications. Restoring missing ENS neurons by stimulating endogenous neuronal regeneration presents a promising therapeutic approach for ENS disease. To reveal the cellular-molecular mechanisms regulating neuronal regeneration we study a species capable of robust ENS restoration, the zebrafish. For this, we developed a chemogenetic ablation model in zebrafish using the Gal4/UAS NTR 2.0 system for targeted ENS neuron ablation. Spatially and temporally controlled neuronal death was confirmed by morphological changes, quantification of neuronal loss, and TUNEL assays. We observed an acute immune response that normalizes at 1 day of treatment. Quantification of regenerated neurons demonstrated complete restoration of ENS neuron numbers to control levels by 9 days post treatment, with recovery of gut motility. Among the regenerated neurons, nitrergic, cholinergic and VIPergic subtypes showed full recovery, whereas serotonergic neurons only displayed partial recovery, indicating subtype-specific differences in regenerative capacity and/or timing of cell replacement. Our study establishes a robust platform for dissecting the cellular-molecular mechanisms of ENS regeneration to develop potential treatment approaches for ENS-related diseases.

Keywords: Enteric neurons, chemogenetic ablation, functional recovery, gut motility, ENS diseases, immune response

Introduction

The enteric nervous system (ENS), the largest subdivision of the peripheral nervous system, consists of an intricate network of neurons and glial cells derived from neural crest progenitors that migrate into the developing gastrointestinal tract (Ganz, 2018; Hao & Young, 2009; Taylor et al., 2016). This complex network plays a pivotal role in regulating essential gastrointestinal functions such as gut motility, nutrient absorption, epithelial secretion, and blood flow (Kuil et al., 2021; Kunze & Furness, 1999; Niesler et al., 2021). Dysfunction or loss of the ENS has been linked to various gastrointestinal disorders such as Hirschsprung disease (HSCR), achalasia, and autism spectrum disorder (Niesler et al., 2021). HSCR, which is characterized by variable degrees ENS neuron loss in the distal gut. HSCR one of the most common congenital anomalies of the ENS, leading to severe intestinal obstruction in neonates, with an estimated incidence of 1 in 5,000 live births (Butler Tjaden & Trainor, 2013). To date, ENS disorders can only be treated symptomatically or by surgical removal of the area with ENS neuron deficits. The current standard treatment for HSCR is surgical resection of the affected gut segment. However, patient outcomes vary widely, and most continue to experience lifelong gastrointestinal defects, highlighting the need for alternative treatments. One of the therapeutic approaches for HSCR is the stimulation of resident stem cells to regenerate missing ENS cells with promising results but varying efficacy depending on the age and the specific gut region (Burns et al., 2016; Joseph et al., 2011; Soret et al., 2020). The successful translation of these approaches requires a comprehensive understanding of the cellular and molecular mechanisms that underlie effective ENS regeneration. Elucidating these mechanisms necessitates the development of a reliable animal model that exhibits robust and reproducible regeneration of ENS neurons following injury.

So far, only a few studies - mostly in mammalian models - have investigated ENS regeneration using chemical, mechanical, or chemical-genetic (chemogenetic) injury. Although these approaches have provided valuable insights, mammalian models show limited and incomplete neuronal regeneration in the ENS (Rueckert & Ganz, 2022; Stavely et al., 2024). In contrast, the zebrafish (*Danio rerio*), a non-mammalian animal model system, is a robust model for studying organ regeneration including various parts of the nervous system such as the brain (Kizil et al., 2012) retina (Hanovice et al., 2019), ENS (El-Nachef & Bronner, 2020; Ohno et al., 2021), but also other organs, such as kidney (Diep et al., 2011), heart (Cao & Poss, 2018), and fin (Romero et al., 2018). Zebrafish also offer numerous experimental advantages, including rapid development, large numbers of offspring, optical transparency that enables live imaging, and a high degree of genetic homology with humans (Howe et al., 2013). Despite these experimental advantages (Kuil et al., 2021; Ganz, 2018), so far, only two studies have studied ENS regeneration in zebrafish using a

69 laser ablation approach (El-Nachef & Bronner, 2020; Ohno et al., 2021). Those studies provided the
70 first evidence that the ENS can regenerate in zebrafish following focal neuronal loss. In particular,
71 Ohno et al., showed that neural crest-derived cells migrate into the ablated region, proliferate, and
72 give rise to new neurons, partially restoring ENS neuron numbers. However, several important
73 issues remain to demonstrate that the ENS fully regenerates in zebrafish: First, the number of
74 regenerated neurons did not reach control levels in the studied time frame. Second, it remains to be
75 shown whether different ENS neuronal subtypes are able to regenerate. Third, it remains unclear
76 whether the regenerated neurons functionally integrated into existing ENS circuits to re-establish
77 normal gut function. In addition, focal laser ablation has several technical limitations, including
78 collateral damage to surrounding tissues, labor-intensive protocols, and restricted ablation of just a
79 few cells within a small gut region, hindering downstream analysis for functional recovery
80 assessment (Ohno et al., 2021).

81 To overcome these challenges, we leveraged an established approach for spatiotemporally
82 controlled cell ablation: the chemogenetic bacterial nitroreductase (NTR) system. This method
83 utilizes the NTR enzyme, which converts prodrugs, e.g., Metronidazole (MTZ), into cytotoxic agents,
84 thereby selectively killing cells that express NTR (Medico et al., 2001). In zebrafish, this
85 chemogenetic method has been successfully applied in regenerative studies by ablating specific cell
86 populations in heart, pancreas, liver, retina, and other organs (Ariga et al., 2010; Curado et al.,
87 2007, Sharrock et al., 2022; White et al., 2017). However, this method has not yet been tested for
88 the ablation of ENS neurons.

89 In this study, we took advantage of the precise spatial-temporal control of the *Gal4/UAS* system
90 (Asakawa et al., 2008; Zhang et al., 2019) for the chemogenetic ablation of ENS neurons in
91 postembryonic zebrafish larvae (**Figure 1A**). We additionally employed the most advanced iteration
92 of the nitroreductase technology, NTR 2.0, which provides effective ablation of target cells at ~10- to
93 100-fold lower concentrations of MTZ than the original NTR system (Sharrock et al., 2022). Using
94 this approach, we establish a robust experimental paradigm of ENS neuron regeneration by ablating
95 only NTR-expressing neurons through MTZ treatment. Morphological and TUNEL analysis
96 confirmed that the ablated cells underwent cell death with a concomitant acute immune response
97 that normalizes within 1 day post treatment (dpt). By 9 dpt, neuronal recovery was complete, with full
98 recovery of most neuronal subtypes, including nitrergic, cholinergic and VIPergic neurons. Our
99 results demonstrate, for the first time, functional recovery of ENS neuron numbers including
100 restoration of gut motility. These findings pave the way for understanding the cellular and molecular

101 mechanisms of ENS regeneration, a first step for developing new therapeutic approaches for
102 gastrointestinal disorders associated with ENS dysfunction in the future.

103

104 **Material and methods**

105 **Animals**

106 All experiments were carried out in accordance with animal welfare laws, guidelines, and
107 policies and were approved by the Michigan State University Institutional Animal Care and Use
108 Committee. Zebrafish lines were maintained in a laboratory breeding colony according to
109 established protocols (Westerfield, 2000). Adult zebrafish were bred naturally in system water,
110 and fertilized eggs were collected and transferred to 100 mm petri dishes containing embryo
111 medium. Embryos were allowed to develop at 28.5°C and staged by days post fertilization (dpf)
112 as described earlier (Kimmel et al., 1995; Webb et al., 2009). The zebrafish lines utilized in this
113 study are listed in **Table 1**. Double transgenic larvae were established to co-express YFP and
114 NTR 2.0 in the ENS neurons. For this, the *Tg(5xUAS:GAP-TagYFP-2A-NTR2.0)jh513Tg*
115 reporter/effector line was maintained together with the *Et(2xNRSE-cfos KALT4)gmc617;*
116 *Tg(5xUAS:GAP-ECFP,he1.1:GAP-ECFP)gmc1913* transgenic fish line. The
117 *Et(2xNRSE:cfos:KalTA4)gmc617* line expresses KalTA4, a zebrafish-optimized Gal4/VP16
118 fusion protein with neuronal specificity (Xie et al., 2012; Sharrock et al., 2022). We confirmed
119 that the *Tg(SAGFF(LF)217B)* drives reporter expression in ENS neurons (described in the
120 results section), as an incross of *Tg(5xUAS:GAP-TagYFP-2A-NTR2.0)*; *Et(2xNRSE-cfos*
121 *KALT4)gmc617; Tg(5xUAS:GAP-ECFP,he1.1:GAP-ECFP)gmc1913* did not show YFP
122 expression in ENS neurons. The *Tg(5xUAS:GAP-ECFP,he1.1:GAP-ECFP)gmc1913* line
123 expresses cyan fluorescent protein (CFP), our analysis was focused on YFP expression driven
124 by the Gal4/UAS system. Genotyping of Gal4 driver lines was performed with the following
125 primers for Gal4 (GAL4F: 5'-CGCTACTCTCCCAAAACCAAAAGG-3'; GAL4R: 5'-
126 TCTCTTCCGATGATGATGTCGCAC -3' using the PCR protocol: 95° x 3 min - [95° x 30s - 60° x
127 30s - 72° x 30s] x 35 - 72° x 5' 12° ∞.

128 **Table 1: Transgenic lines used in this study**

Full name	Abbreviation	Source
Tg(SAGFF(LF)217B)	*217B:Gal4*	Asakawa et al., 2008
Tg(SAGFF(LF)234A)	*234A:Gal4*	Asakawa et al., 2008
Tg(gSAIzGFFM495A)	*495A:Gal4*	Asakawa et al., 2008
Tg(5xUAS:EGFP)nkuasgfp	*UAS:GFP*	Kawakami et al., 2010
Tg(UAS-E1b:NfsB-mCherry)c264	*UAS:NTR-mCherry*	Davison et al., 2007

Full name	Abbreviation	Source
Tg(5xUAS:GAP-TagYFP-2A-NTR2.0)jh513Tg; Et(2xNRSE-cfos KALT4)gmc617; Tg(5xUAS:GAP-ECFP, he1.1:GAP-ECFP)gmc1913	*UAS:YFP-NTR 2.0**	Sharrock et al., 2022; Xie et al., 2012

*The *Tg(5xUAS:GAP-TagYFP-2A-NTR2.0)jh513Tg* fish were maintained together with the *Et(2xNRSE-cfos KALT4)gmc617; Tg(5xUAS:GAP-ECFP,he1.1:GAP-ECFP)gmc1913* lines.

Chemogenetic ablation using Metronidazole

The *217B:Gal4* driver line was crossed with the *UAS:YFP-NTR 2.0* responder line. Offspring from this cross were sorted based on YFP+ cells in the gut into YFP+ and YFP− groups at 5 dpf using a Zeiss Axio ZoomV16 fluorescent stereo microscope. The sorted larvae were then treated at 5 dpf or for the later time points transferred to the nursery until the day of the assay. Prior to MTZ treatment, larvae - except for the 5 dpf groups - were starved for 24 hours to clear the gut of autofluorescent matter. Approximately 50 larvae were transferred to a petri dish (100 mm × 15 mm) containing 40 mL of 400 µM MTZ (M1547 Sigma Aldrich) (Sharrock et al., 2022) in zebrafish system water (diluted from a 5 mM stock solution). The following experimental groups were used: 1) YFP+ MTZ (YFP+ larvae treated with MTZ; 2) YFP+ control (YFP+ larvae, not treated with MTZ); and 3) YFP- MTZ (YFP- larvae, treated with MTZ). Larvae were incubated in the dark for 24 hours to ensure maximal drug exposure as MTZ is light sensitive. After 24 hours, the effects of MTZ treatment on YFP+ cell ablation were assessed using a Zeiss Axio Zoom.V16 fluorescent stereo microscope. After confirmation of cell loss, the MTZ solution was discarded and larvae were returned to the nursery, placed in 2.8-liter tanks (~40 larvae per tank), and raised until the 21 dpt / 33 dpf.

ENS neuron regeneration analysis

The regeneration of MTZ-treated YFP+ cells in the gut was assessed at 12 dpf (0 dpt, before ablation) and subsequently at three-day intervals from 13 dpf (1 dpt) to 27 dpf (15 dpt) and compared to YFP+ untreated controls. At each regeneration time point, both control and treated larvae were checked briefly using a Zeiss Axio Zoom.V16 fluorescent stereo microscope, then fixed and immunoassayed (as described below) by confocal microscopy imaging for data acquisition.

Sample fixation

To ensure optimal imaging conditions, larvae were fasted for 24 hours prior to sampling at the required stages to allow for gut clearance of autofluorescent matter. Then, larvae were

160 euthanized with an overdose of Tricaine Methanesulfonate (MS-222). **For immunolabeling**,
161 euthanized samples were fixed in 4% paraformaldehyde (PFA) prepared in 1x sweet buffer (8%
162 sucrose, 0.2 M $CaCl_2$, 0.2 M PO_4 buffer, pH 7.3) for 2 hours at room temperature. Then, they
163 were washed subsequently 2 times in 0.5% Phosphate buffer saline-Triton™ X-100 (PBSTX) for
164 15 mins at room temperature, and stored in PBSTX at 4°C**. For TUNEL assay**, euthanized
165 samples were fixed overnight in 10% Natural buffer saline (NBF) at 4°C, then washed three
166 times in PBS for 5 minutes at room temperature and stored in PBS at 4°C. **For Hybridization**
167 **Chain Reaction (HCR)**, euthanized larvae were rinsed thoroughly in RNAase free water, and
168 fixed in RNAase free 4% PFA in PBS at 4°C for ~16 hours, washed three times in PBS for 5
169 minutes at room temperature, dehydrated in a graded methanol series (50, 70, 90, 95 and 100
170 % methanol in nuclease free water), and stored in 100% methanol at −20°C for a minimum of
171 16 hours or up to six months (Ibarra-García-Padilla et al., 2021).
172
173 **TUNEL assay**
174 TUNEL assays were performed using the Click-iT™ Plus TUNEL Assay Kits (C10618, Thermo
175 Fisher Scientific) for In Situ Apoptosis Detection. For this, PBS was removed from fixed samples
176 and permeabilization was carried out using Proteinase K (20 µg/mL) for 50 minutes at room
177 temperature, followed by three PBS washes and a deionized water rinse. Then samples were
178 re-fixed in 10% NBF in PBS for 5 minutes at 37°C, followed by three additional PBS washes and
179 another deionized water rinse. To detect DNA strand breaks (i.e., for the positive control), the
180 larvae were incubated in 1 unit of DNase I (Cat. No. 18068-015) diluted into 1× DNase I
181 Reaction Buffer for 30 minutes at room temperature (**Figure S1)**. After that, larvae were
182 preincubated in 150 µL of Terminal deoxynucleotidyl transferase (TdT) buffer for 10 minutes at
183 37°C, incubated in the 100 µL TdT reaction mixture {94 µL TdT Reaction Buffer, 2 µL 5-ethynyl-
184 2'-deoxyuridine-5'-triphosphate (EdUTP), and 4 µL TdT enzyme} for 30 minutes at 37°C, rinsed
185 in deionized water, washed twice in 3 % bovine serum albumin (BSA) in 0.1% PBS-Triton™ X-
186 100 for 5 minutes each, and one time in PBS. Then the larvae were incubated with the reaction
187 cocktail (90 µL TUNEL Supermix and 10 µL 10× Click-iT Plus TUNEL Reaction Buffer Additive)
188 for 30 minutes at 37°C in the dark, followed by two 3% BSA in PBS washes and two final PBS
189 washes. TUNEL staining was assessed using a Zeiss Axio Zoom.V16 fluorescence
190 stereomicroscope. Immunostaining was subsequently performed under dark conditions, as
191 described below, and larvae were stored in PBS until imaging.
192
193 **Immunostaining**

194 Whole-mount immunostaining was performed as previously described (Bandla et al., 2022;
195 Uyttebroek et al., 2010). The following primary antibodies: 5-HT (1:5,000, catalog number
196 20080), HuC/D (1:1,000, catalog number A-21271), mouse GFP (1:300, catalog number
197 A11120), rabbit GFP (1:1,000, catalog number A11122), nNOS (1:1,000, catalog number
198 GTX133407) and L-plastin, Lcp1 (1:100, catalog number GTX124420) were utilized to perform
199 immunostaining. The primary antibodies were detected using Alexa Fluor 488 and/or 568
200 secondary antibodies, followed by washes with 0.3% PBSTX. The staining was assessed using
201 Zeiss Axio Zoom.V16 fluorescent stereo microscope and samples were stored in 0.3% PBSTX
202 at 4°C until imaging.
203
204 **Hybridization Chain Reaction**
205 The (HCR) kit, probes, *vip* (Accession number: NM_001114553.3) and *slc18a3a* (Accession
206 number: NM_001077550.1), and hairpins were from Molecular Instruments, Inc.
207 (https://www.molecularinstruments.com) and the HCR protocol was performed as previously
208 described (Ibarra-García-Padilla et al., 2021) with minor modifications. The HCR protocol was
209 followed by immunostaining. The fixed samples stored in 100% methanol were rehydrated in
210 graded methanol series, permeabilized with pre-chilled acetone at −20°C for 25 min, treated
211 with 20 µg of Proteinase K for 1 h at room temperature, refixed in 4% PFA in PBS for 20 min,
212 and washed with PBS-Tween before hybridization. For HCR hybridization, samples were pre-
213 hybridized at 37°C, incubated with a probe mixture (4 µL of each 1 µM probe set stock) for 12–
214 16 hours, washed to remove excess probes, and amplified for 12–16 hours, followed by
215 sequential washes (Ibarra-García-Padilla et al., 2021). For antibody staining, samples were
216 blocked in 5% goat serum, incubated with primary anti-mouse GFP (1:300, catalog number
217 A11120) antibodies overnight at 4°C, washed extensively, and incubated with secondary
218 antibodies overnight (Ibarra-García-Padilla et al., 2021). Throughout the protocol, samples were
219 protected from light to prevent photobleaching, ensuring optimal visualization of hybridization
220 and staining results. Afterward, stained samples were stored in PBST at 4°C until imaging.
221
222 **Imaging, data acquisition, and quantification**
223 For analysis of colocalization and quantification, intestines were dissected with forceps and
224 mounted on glass slides in 0.3% PBSTX or Fluoromount-G® mounting media (Southern Biotech,
225 catalog number 0100-01) and covered with a coverslip. For the analysis of Gal4-based reporter
226 co-expression with the pan-neuronal marker HuC/D, mounted intestines were imaged on a
227 Zeiss Axio Imager microscope operated through the ZEN software to determine colocalization.

228 Confocal z-stacks images were captured using the 3i spinning disk confocal microscope with a
229 10, 20, or 60× objectives, operated through Slidebook6 software (Version 6.0.13). For cell
230 quantification, z-stacks were generated from confocal stacks in Slidebook6, which were used for
231 manual cell counts and colocalization analysis. For analysis within gut regions, the images of
232 the intestine were divided into three sections - anterior, middle, and posterior - as previously
233 described (Jianlong Li et al., 2020; Wallace et al., 2005). Cell counts were normalized to 200 μm
234 to account for varying lengths of each of gut regions between larvae and to 1000 μm for the
235 whole gut.
236
237 **Analysis of neuron morphology**
238 To analyze morphological changes in neurons after MTZ exposure, control and MTZ-treated
239 larvae were euthanized at the timepoint indicated, their intestines were dissected, mounted on
240 glass slide in PBS and imaged on the 3i spinning disk confocal microscope with a 60× objective,
241 operated through Slidebook6 software (Version 6.0.13).
242
243 **Gut anterograde movements analysis**
244 Larvae from control and treated groups were fasted 24 hours prior to analysis, anesthetized with
245 MS-222, and embedded in 0.8% low-melting-point agarose. Videos of the gut region from
246 midgut to posterior were recorded on the Zeiss Axio Zoom.V16 fluorescent stereo microscope
247 with ZEN Imaging Software (ZEN 2.3 blue edition). All time lapse videos were recorded using
248 the same conditions, including exposure time (206s), frame rate (100 frames / 206 sec), and
249 pixels (2752 x 2208). The total number of anterograde, peristaltic wave movements was
250 analyzed from the recorded videos. The Peristaltic Wave Interval (PWI) time was calculated as:
251 PWI = T/N where PWI represents the average time interval (in seconds) between two
252 consecutive anterograde peristaltic movements. The total duration of each video (T, in seconds)
253 and the total number of peristaltic movements observed (N) were recorded.
254
255 **Statistical Analysis**
256 For multiple comparisons, one-way and two-way ANOVA were applied to normally distributed
257 data, while the non-parametric Kruskal–Wallis test was used for non-normally distributed data.
258 For pairwise comparisons, unpaired t-tests were used for normally distributed data, and the
259 Mann–Whitney test was used for non-normally distributed data. To evaluate temporal changes
260 across multiple time points in regeneration studies, multiple unpaired t-tests were performed
261 between MTZ-treated and control larvae. For fractional analysis of neuronal colocalization

262 patterns, descriptive statistics were applied. Fold-change analysis was calculated based on the
263 average number of cells in each group. All statistical analyses were performed using GraphPad
264 Prism 9.1 (GraphPad Software, San Diego, CA, USA). A significance threshold of $p < 0.05$ was
265 used to determine statistically significant differences.
266
267 **Results**
268 **Identification of Gal4 driver line for specific ablation of ENS neurons**
269 To identify a Gal4 driver line for maximizing the breadth and selectivity of ENS neuron ablation,
270 we crossed three Gal4 gene-trap driver lines (*495A:Gal4; 234A:Gal4; 217B:Gal4*) with a *UAS*
271 reporter line to analyze the extent and specificity of reporter gene expression in the ENS and
272 surrounding tissues. To determine if reporter gene expression within the ENS is primarily
273 restricted to neurons, thereby minimizing off-target ablation, we investigated reporter gene co-
274 expression with the pan-neuronal marker HuC/D in the ENS at 5 dpf (*495A:Gal4xUAS:GFP*,
275 *234A:Gal4xUAS:NTR:DsRed*) and at 5, 6 and 7 dpf (*217B:Gal4xUAS:GFP*) (**Figure 1**).
276 Our analysis revealed notable differences in the co-expression profiles among the driver lines.
277 The *495A:Gal4* line has previously been reported to show largely gut-restricted expression, but
278 which gut cells express the reporter had not been determined (Kawakami et al., 2010). We
279 found that the intestines of the *495A:Gal4* line displayed only about half HuC/D+/Reporter+ cells
280 with many reporter+ cells being HuC/D- and HuC/D+/Reporter- cells (**Figure 1B**). The
281 expression of *234A:Gal4* has been reported to be expressed in the ENS, but also broadly
282 outside the gut (Kawakami et al., 2010; Heanue et al., 2016). In contrast, the *217B:Gal4* had
283 been reported to have reporter expression in the gut with minimal expression outside the gut
284 compared to the *234A:Gal4* line. Consistent with these reports, we found that both *234A:Gal4*
285 and *217B:Gal4* driver lines exhibited higher number of neurons co-expressing HuC/D+ and
286 Reporter with only a small population of HuC/D-/Reporter+ and HuC/D+/Reporter- cells (**Figure**
287 **1B-C**).
288 Comparatively, both the *234A:Gal4* and *217B:Gal4* lines had sufficient Reporter+ cells in the
289 gut. However, *234A:Gal4* drives extensive reporter gene expression outside the ENS and in
290 ENS progenitor cells (Heanue et al., 2016), which would lead to ablation of additional, non-
291 targeted cells. Therefore, we chose the *217B:Gal4* line to maximize the extent and specificity of
292 ENS neuron ablation (**Figure 1C**).
293
294

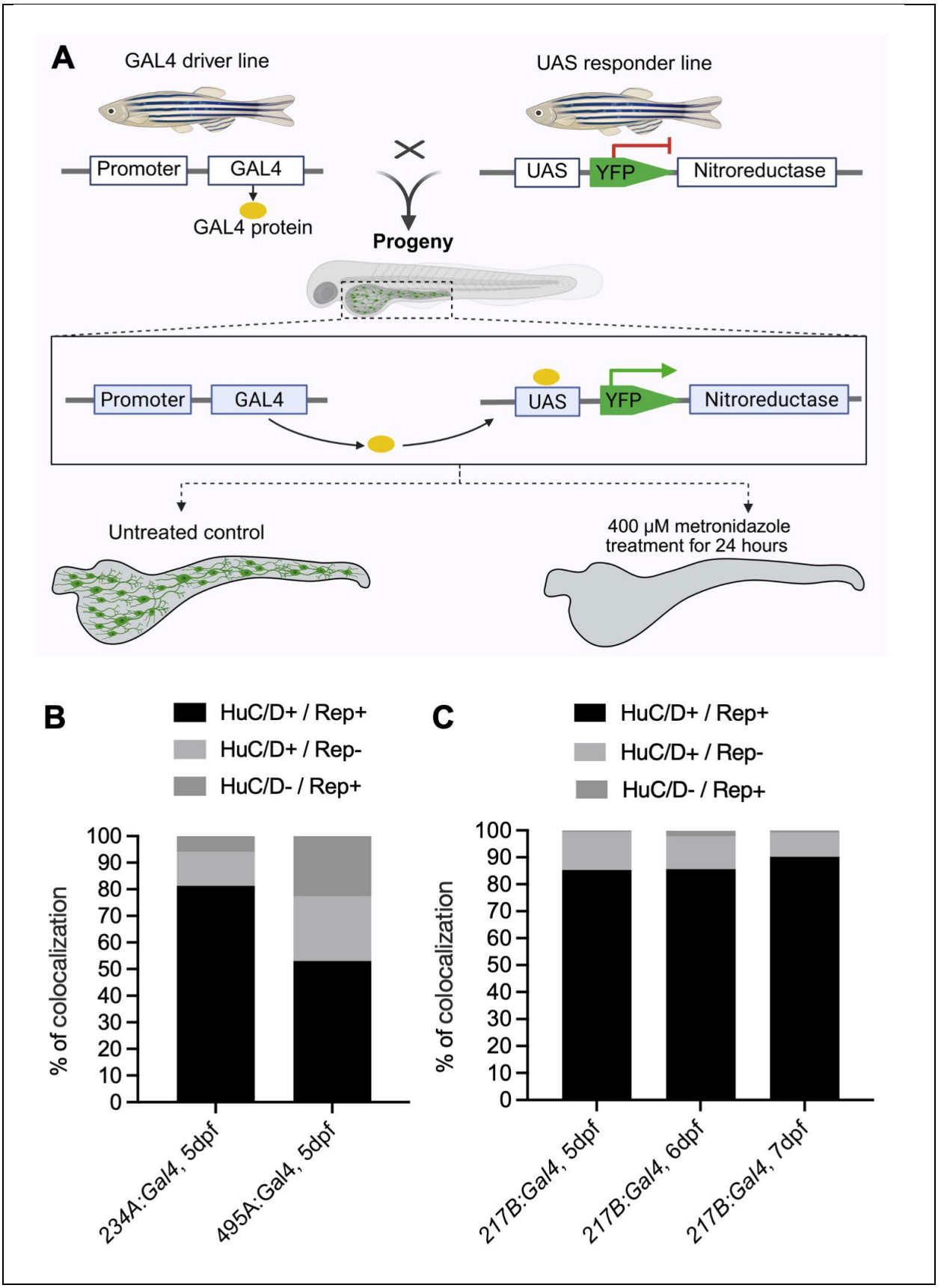
A
GAL4 driver line
UAS responder line
Promoter
GAL4
GAL4 protein
UAS
YFP
Nitroreductase
Progeny
Promoter
GAL4
UAS
YFP
Nitroreductase
Untreated control
400 μM metronidazole
treatment for 24 hours
B
HuC/D+ / Rep+
HuC/D+ / Rep-
HuC/D- / Rep+
% of colocalization
100
90
80
70
60
50
40
30
20
10
0
234A:Gal4, 5dpf
495A:Gal4, 5dpf
C
HuC/D+ / Rep+
HuC/D+ / Rep-
HuC/D- / Rep+
% of colocalization
100
90
80
70
60
50
40
30
20
10
0
217B:Gal4, 5dpf
217B:Gal4, 6dpf
217B:Gal4, 7dpf

Figure 1. Identification of a Gal4 driver line for efficient ENS neuron ablation using a chemogenetic system. (A) Pictorial representation of chemogenetic ablation of ENS neurons. A carrier of the Gal4 driver line, *Tg*(*Gal4)*, which drives expression in ENS neurons was crossed with a carrier of the responder/effector line *Tg(UAS:YFP-NTR 2.0)*, where the Gal4 protein binds to Upstream Activating Sequence (*UAS*) element, initiating expression of both *yellow fluorescence protein* (YFP, reporter protein) and *nitroreductase* (NTR 2.0). Left side: Schematic representation of the untreated control intestine, where enteric neurons co-expressing the *Gal4* and *UAS* transgenes also express both YFP and NTR 2.0 in ENS neurons (green). Right side: Schematic representation of intestine following treatment with 400 μM metronidazole (MTZ). The prodrug MTZ is enzymatically converted by NTR 2.0 into a cytotoxic compound, leading to the selective ablation of YFP-NTR 2.0-expressing enteric neurons. The bar graphs show colocalization percentage of the pan-neuronal marker HuC/D with Reporter (Rep) expression within the gut for Gal4 driver. **(B)** For the *234A:Gal4* line, most Rep+ cells are HuC/D+ at 5 dpf (81.3% HuC/D+/Rep+). The remaining cells consist of 12.7% HuC/D+/ Rep- and 6.0% HuC/D-/Rep+ (n = 12 larvae per group, 2 experiments). For the *495A:Gal4* line, only 55% cells are HuC/D+/Rep+ at 5 dpf, the remaining cells are 23.5% HuC/D+/ Rep- and 21.2% HuC/D-/Rep+ (n = 12 larvae per group, 2 experiments). **(C)** For the *217B:Gal4* line, there is a high degree of overlap between Rep and HuC/D expression [(85.3% (5 dpf), 85.7% (6 dpf), and 90.2% (7 dpf)]. The remaining cells consist of HuC/D+/ Rep- [14% (5 dpf) 12.3% (6 dpf) and 9.0% (7 dpf)] and HuC/D-/Rep+ [0.7% (5 dpf), 2.0% (6 dpf), and 0.8% (7 dpf)], n = 13 (5 dpf), 15 (6 dpf), and 14 (7 dpf) larvae per group, 2 experiments per time point. dpf = days post fertilization.

295

296 **Establishing a robust chemogenetic ablation assay for ENS neuron**

297 To establish a robust ENS neuron ablation assay, we used offspring from a cross between the
298 *217B:Gal4* and *UAS:YFP-NTR 2.0* transgenic lines that co-express YFP and NTR 2.0 in cells in
299 the gut (YFP+). To ablate YFP-NTR 2.0 expressing cells, we treated YFP+ larvae with 400 μM
300 MTZ for 24 hours (Sharrock et al., 2022) starting at 5 or 12 dpf. To assess the extent of ENS
301 cell loss, we quantified YFP+ cells at 6 dpf and 13 dpf (1 dpt for MTZ-treated larvae). In
302 untreated controls, no significant difference in YFP+ cells was observed between 5 and 6 dpf, or
303 12 and 13 dpf. Conversely, MTZ-treated groups showed a near-complete loss of YFP+ cell
304 numbers at 1 dpt compared to 0 dpt (before treatment) and untreated control (**Figure 2A-C**).
305 As 24 h of MTZ treatment showed robust YFP+ cell ablation at both developmental stages, we
306 decided to move forward with MTZ treatment at 12 dpf for further analyses. Embryonic

307 neurogenesis is still very active at 5 dpf (Olden et al., 2008; Roy-Carson et al., 2017). Therefore,
308 ablating neurons at 5 dpf might include processes of developmental neurogenesis rather than of
309 neuronal regeneration, which we aimed to avoid.
310 To confirm that YFP+ cells are neurons at 12 dpf, we analyzed co-expression of YFP and
311 HuC/D in *217B:Gal4*; *UAS:YFP-NTR 2.0* fish. Quantification revealed that, on average, 44.4
312 YFP+ neurons were observed among a total of 204.6 HuC/D+ neurons. We found that 96.3% of
313 YFP+ cells were HuC/D+ indicating that the vast majority of YFP+ cells are ENS neurons while
314 only 3.7% YFP+ cells are HuC/D-. Therefore, we will hereafter refer to YFP+ cells in these lines
315 as YFP+ neurons (**Figure 2D-F**).
316

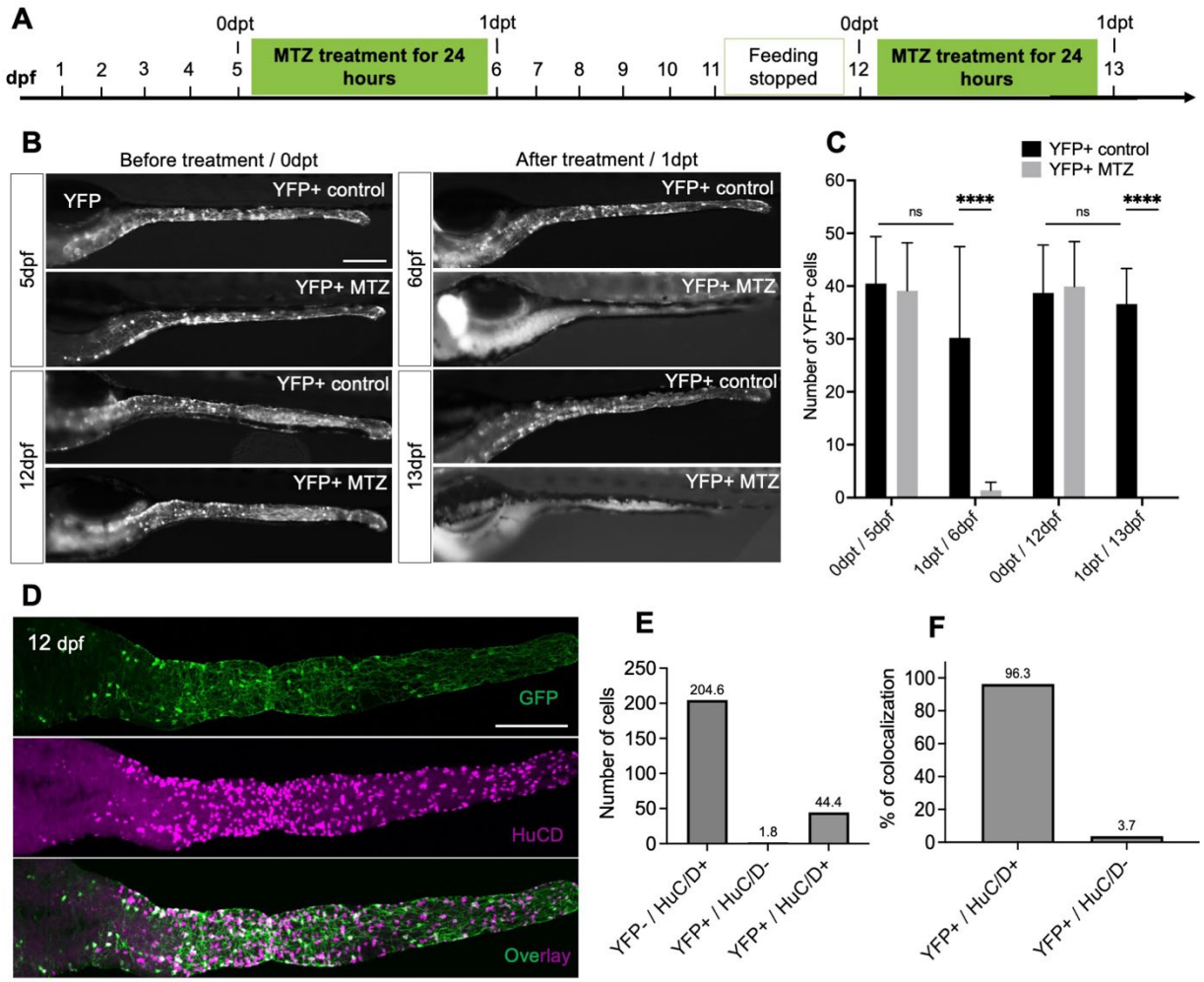

Figure 2. Establishment of a robust ENS neuron ablation assay. (A) The timeline of dpf and dpt illustrates the experimental procedure for MTZ treatments initiated at either 5 or 12 dpf. **(B)** Whole-mount side views of live larval guts at the stage indicated. Left panel: YFP+

neurons (white dots) are present before treatment (0 dpt) at 5 or 12 dpf in YFP+ larvae. Right panel: after 24 hours treatment with 400 μM Metronidazole (MTZ), YFP+ cells are completely absent in MTZ-treated fish (YFP+ MTZ) but present in untreated controls (YFP+ control). **(C)** Quantification of YFP+ neurons in control and MTZ-treated groups. Data are shown as mean ± SD (n = 10 larvae per group, 2 experiments); statistical significance ****$p < 0.0001$; ns = non-significant. **(D)** At 12 dpf, YFP+ cells [(anti-GFP immunostaining (top, green)] and the pan-neuronal marker HuC/D+ cells (middle, magenta) highly colocalize (bottom, overlay). **(E)** Quantification of GFP+/HuC/D+, GFP+/HuC/D- and GFP-/HuC/D+ cells. Data are shown as mean (n= 10 larvae per group, 2 experiments). **(F)** Percentage of YFP+ cells that are HuC/D+ and HuC/D- cells in **E**. (D) Maximum projection confocal images of dissected intestine at 12 dpf; dpf = days post fertilization. dpf = days post fertilization; dpt = days post treatment; SD = standard deviation; Scale bar = 100 μm.

YFP+ neurons undergo DNA-damage induced cell death after MTZ treatment

To determine the timeline of neuronal ablation, we quantified number of YFP+ neurons at 6, 12 and 24 hpt. We find that YFP+ neurons are essentially absent at 24 hpt indicating that MTZ-induced ablation of YFP+ neurons is completed within 24 hours post-treatment (**Figure S2**). To test if YFP+ neurons undergo cell death after MTZ treatment, we evaluated changes in neuronal morphology and performed TUNEL assays to detect cells undergoing cell death. YFP+ neurons in untreated control larvae displayed normal morphology with no visible signs of morphological changes (**Figure 3A**). In contrast, YFP+ neurons in MTZ-treated samples exhibited significant morphological changes, including axonal and cell body fragmentation and retraction of neuronal processes, consistent with neurons undergoing cell death [**Figure 3**, (Cusack et al., 2013; Ham et al., 2010)]. Additionally, we conducted TUNEL assays combined with immunostaining for YFP to assess DNA damage in control and MTZ-treated fish 6 at hpt. As expected, we found GFP+/TUNEL+ cells in both treated and control groups since apoptotic cell death is a natural ongoing process at 12 dpf (Lee et al., 2023). However, significantly higher numbers of GFP+/TUNEL+ cells were observed in the MTZ-treated group compared to YFP+ untreated control (**Figure 3B, C**). In addition, GFP+/TUNEL+ neurons exhibited clear morphological changes indicating that YFP+ neurons were undergoing cell death (**Figure 3D**). These results indicate that MTZ treatment induces DNA damage which leads to cell death with pronounced structural alterations attending this process, consistent with prior studies using this system for selective cell death (Kulkarni et al., 2018; White & Mumm, 2013).

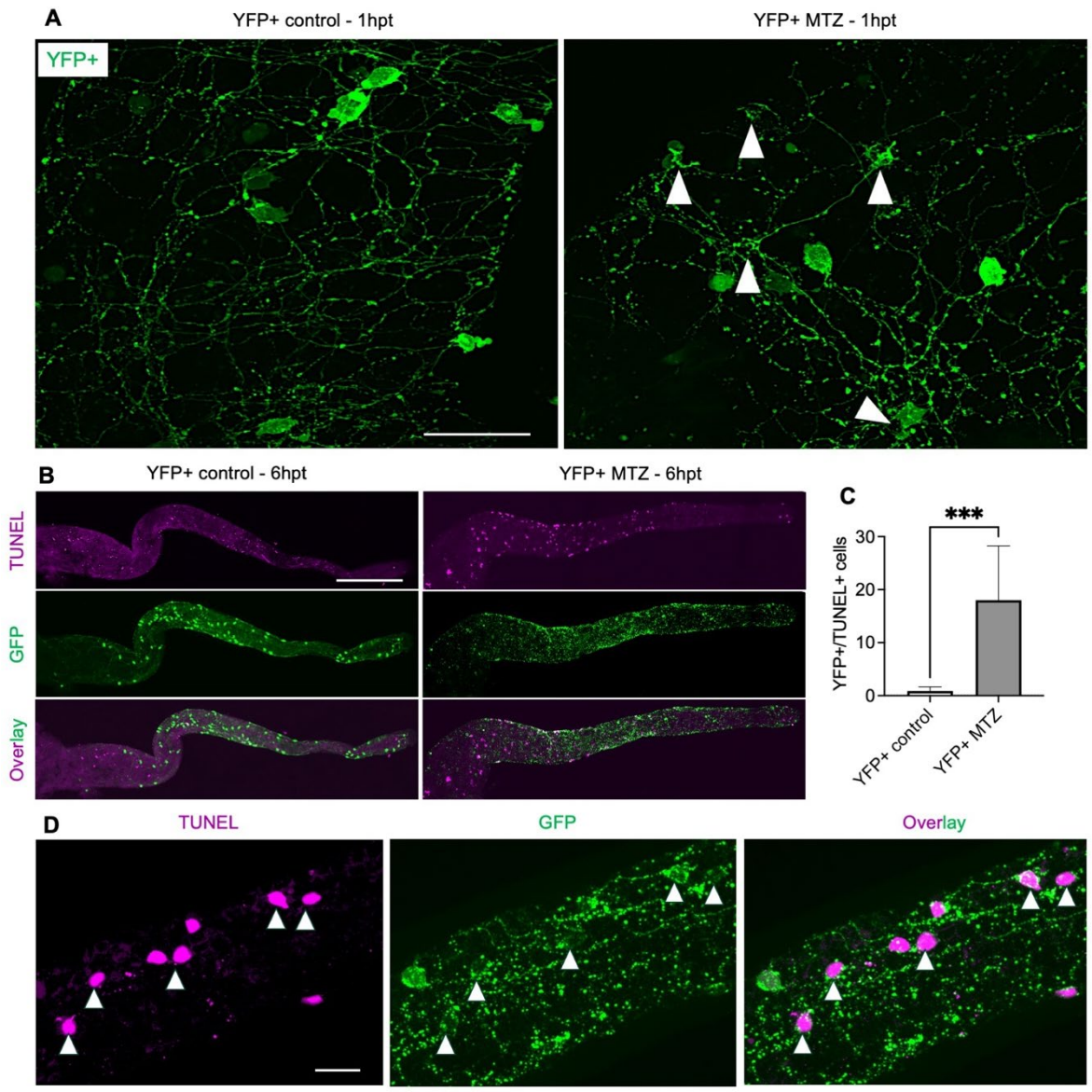

Figure 3. MTZ treatment induces DNA-damage cell death in YFP+ neurons. (A) In 12 dpf larvae, YFP+ neurons displays normal neuronal morphology in the untreated control group, while MTZ treated YFP+ neurons show fragmented and retracted neuronal processes at 1 hpt (white arrowheads; n=6 larvae per group, 2 experiments). **(B)** At 6 hpt, there is an increase in TUNEL staining (magenta) in YFP+ neurons (anti-GFP immunostaining) in MTZ treated larvae compared to untreated controls. In YFP+ control group, GFP+ neurons have normal morphology. In contrast, GFP+ neurons in the MTZ-treated group show fragmented morphology indicative of cell death. **(C)** Quantification of GFP+/TUNEL+ cells shows significant increase in YFP+ MTZ-treated larvae compared to YFP+ untreated control. Data are shown as mean ± SD (n= 9 larvae per group, 2

experiments); statistical significance ***$p < 0.001$. **(D)** Magnified images of GFP+/TUNEL+ cells (white arrowhead) in the YFP+ MTZ-treated group. **(A-D)** Maximum projection confocal images of dissected intestines at 1 hpt **(A)** and 6 hpt **(B, D)**. dpf = days post fertilization; hpt = hours post treatment; Scale bars = 20 µm in A; 100 µm in B; 40 µm in D.

339

340 **MTZ-induced YFP+ cell ablation elicits acute immune cell activation**

341 Immune cell activation plays a crucial role in neuronal regeneration (Kyritsis et al., 2012; White
342 et al., 2017). To determine whether MTZ-induced cell ablation stimulates an immune response,
343 we analyzed immune cells dynamics using the pan-leukocyte marker L-plastin (Hiroto
344 Shinomiya, 2012). In YFP- MTZ-treated (non-ablated) and YFP+ MTZ-treated (ablated) larvae,
345 we quantified L-plastin+ cell numbers in gut across the time points of neuronal cell death (6 hpt,
346 12 hpt, and 1 dpt; see **Figure S2**). At 6 hpt, YFP+ MTZ-treated larvae exhibited a significant
347 increase in L-plastin+ cells compared with YFP- MTZ-treated larvae. By 12 hpt and 1 dpt, no
348 significant differences were detected (**Figure 4A, B**). Consistently, fold-change analysis
349 revealed a peak in L-plastin+ cell numbers at 6 hpt, which steadily declined back to normal
350 levels by 1 dpt (**Figure 4C**). These findings indicate that MTZ-induced ablation of YFP+ cells
351 trigger a transient immune response in the gut, characterized by an acute accumulation of L-
352 plastin+ cells that resolves within 24 hours.

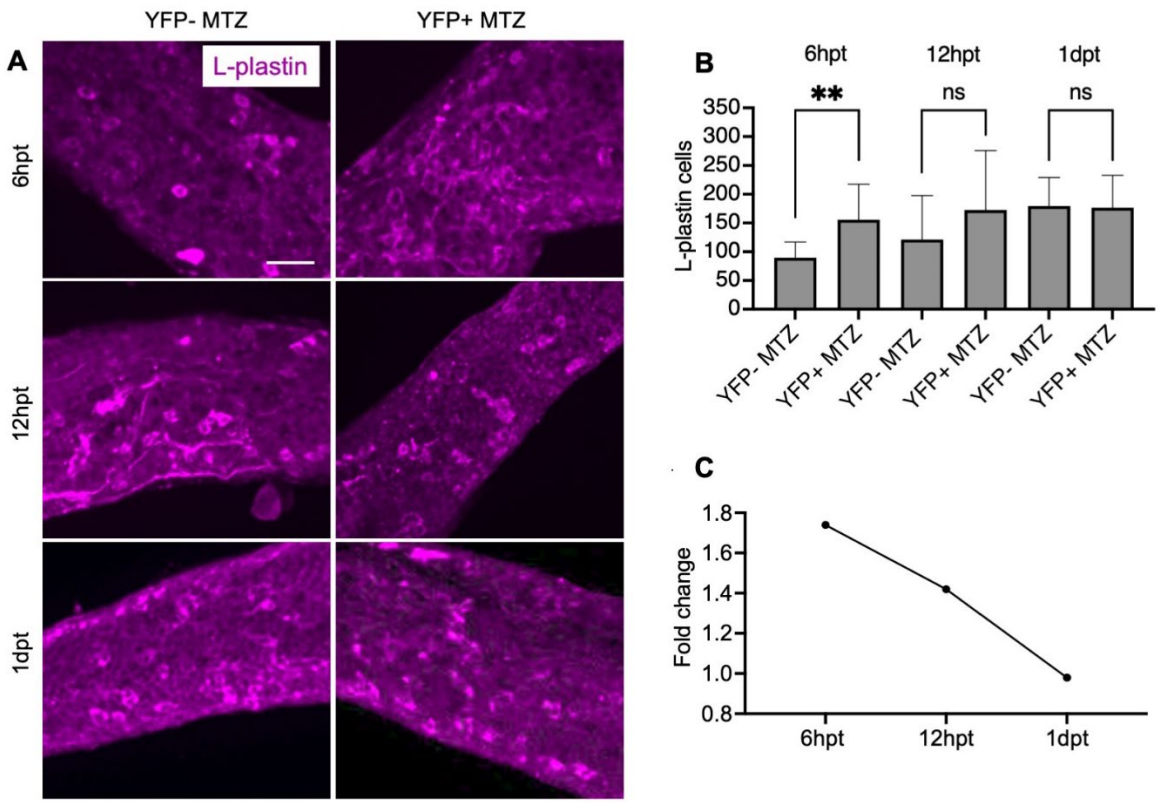

Figure 4. L-plastin+ immune cells increase rapidly after YFP+ cell death in the gut. **(A)** L-plastin+ immune cells (magenta) in YFP- MTZ (non-ablated) and YFP+ MTZ (ablated) larvae at 6 hpt, 12 hpt, and 1 dpt. **(B)** Quantification of L-plastin+ cells at indicated time points. At 6 hpt, YFP+ MTZ groups shows a significant increase in L-plastin+ cells in the gut compared with YFP- MTZ. No significant difference (ns) was detected at 12 hpt and 1 dpt. **(C)** Fold-change analysis of L-plastin+ cell numbers in YFP+ MTZ larvae relative to YFP- MTZ larvae across time points shows a peak at 6 hpt followed by a decline to baseline levels by 1 dpt. **(A)** Maximum projection confocal images of dissected intestines at time point indicated. Data are shown as mean ± SD (n= 10 larvae per group, 2 experiments); Statistical significance: $^{**}p < 0.01$; ns = no significant difference; hpt = hours post treatment; dpt = day post treatment; Scale bar = 50 μm.

353
354
355
356
357
358

359 **YFP+ neurons regenerate following targeted ablation**
360 Next, we investigated whether YFP+ neuron numbers were restored to control levels, which
361 would indicate that they regenerate after MTZ treatment. We quantified YFP+ neurons along the
362 whole gut at different time points before and after treatment in YFP+ MTZ and YFP+ control
363 larvae. YFP+ control larvae exhibited an obvious neuronal network from 0 to 15 dpt (**Figure 5A-**
364 **B**). In contrast, YFP+ neuronal numbers were reduced in the YFP+ MTZ larvae at 1 dpt,
365 confirming successful ablation of YFP+ neurons (**Figure 5A-B**). By 2 dpt, we find a small
366 number of YFP+ neurons along with developing neurites that bridge across the gut (**Figure S3**).
367 YFP+ neuron numbers continue to increase, but through 6 dpt there was a significant difference
368 in YFP+ numbers compared to the control group. By 9 dpt, regenerated YFP+ neuron numbers
369 reached levels comparable to the controls and remained at control levels through 12 and 15 dpt
370 (**Figure 5A-B**). We noticed that approximately half of the YFP+ MTZ larvae exhibited abnormal
371 body posture after 9 dpt. This phenotype might be caused by off-target ablation of reporter-
372 positive cell in the spinal cord area (**Figure S4**). To investigate whether this affected YFP+
373 neuron regeneration, we compared regenerated YFP+ neuron counts in larvae with normal
374 posture and those with defective posture at 12 dpt but found no significant difference (**Figure**
375 **S5**). This indicates that postural defects did not impact neuron regeneration. To determine if
376 there were differences in the timeline of neuron regeneration within discrete gut regions
377 compared to the whole gut, we quantified YFP+ neurons in three main gut regions - anterior,
378 midgut, and posterior (Jianlong Li et al., 2020; Wallace et al., 2005). We found that the timeline
379 of YFP+ neuron regeneration was the same in the three gut regions as in the whole gut (**Figure**
380 **5C, B-F**).
381 As shown above, YFP+ neurons colocalized with a small subset of HuC/D+ neurons, indicating
382 that only a fraction of ENS neurons were ablated (**Figure 2D-F**). To assess if ablation of YFP+
383 neurons has any effects on the YFP- ENS neuronal population, we quantified HuC/D+ neurons
384 in YFP+ MTZ and YFP+ control groups at 0 dpt (before treatment) and 1 and 3 dpt. We found
385 no significant difference in HuC/D+ neuron numbers between treated and control groups after
386 ablation of YFP+ neurons (**Figure S6A-D**). This lack of significance may be due to the relatively
387 small proportion of YFP+ neurons within the total HuC/D+ population—on average, 44.4 out of
388 204.6 neurons (**Figure 2F**). Additionally, MTZ treatment alone in YFP- MTZ treated larvae did
389 not significantly decrease overall HuC/D numbers (**Figure S6E**).
390
391
392

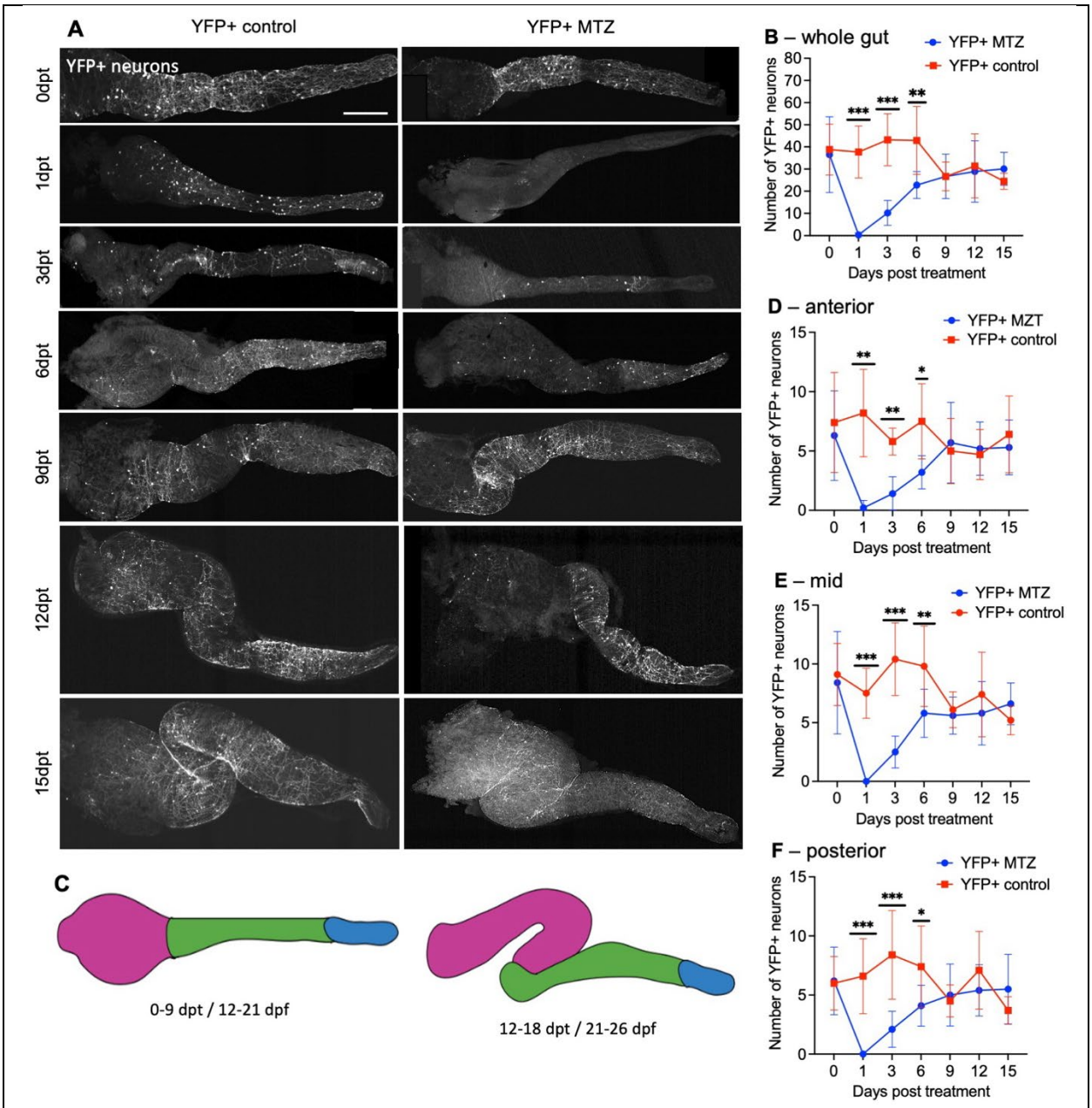

Figure 5. Timeline of YFP+ neuron regeneration in the whole intestine and defined gut regions.

(A) YFP+ neurons (labelled with anti-GFP antibody) and the neuronal network in YFP+ control and YFP+ MTZ zebrafish larvae at 0 (before treatment) and 1, 3, 6, 9, 12, and 15 dpt. **(B)** YFP+ control larvae exhibited consistent GFP+ neuron numbers till 6 dpt with a slight decrease by 9 through 15 dpt. In contrast, the YFP+ MTZ group showed a dramatic decrease in YFP+ neurons, confirming complete ablation of YFP+ neurons ($p < 0.001$) at 1 dpt. A small number of YFP+ neurons appeared by 3 and 6 dpt, but YFP+ neuron numbers were still

significantly decreased compared to the control. By 9 dpt, neuronal number fully recovered with no significant difference between treated and controls at 9, 12 and 15 dpt. **(C)** Schematic representation of the zebrafish gut regions shows the three analyzed gut regions (magenta = anterior, green = midgut, blue = posterior) at 0–9 dpt and 12–18 dpt based on Jianlong Li et al. (2020) and Wallace et al. (2005). Anterior **(D)**, mid **(E)** and posterior **(F)** gut regions show the same timeline of YFP+ neuron regeneration as the whole gut **(B)**. **(A)** Maximum projection confocal images of dissected intestines at time point indicated; Data are presented as mean ± SD (10 larvae per group, 2 experiments); Statistical significance: ***$p < 0.001$, **$p < 0.01$ and *$p < 0.05$; dpt = days post treatment; Scale bar = 100 µm.

Specific co-expressed neuronal subtypes regenerate following ablation

The ENS is composed of various neuron subtypes which control the different functions of the gut including gut motility (Holmberg et al., 2006; Roach et al., 2013; Uyttebroek et al., 2010). The subtypes can be grouped into three main classes which include nitrergic/VIPergic inhibitory motor neurons [neuronal nitric oxide synthase+ (nNOS+); *vasoactive intestinal peptide*+ (*vip*+)], cholinergic excitatory motor neurons [*solute carrier family 18 member 3a*+ *slc18a3a*+)], and serotonergic neurons [5-hydroxytryptamine+, 5-HT+)] (Kuil et al., 2023; Li et al., 2025; Uyttebroek et al., 2010). To determine the neuronal subtype composition within the YFP+ neuronal population, we analyzed co-expression of these subtype markers with YFP at 12 dpf, prior to MTZ treatment. At 0 dpt, we found that 57.54%, 12.26%, 13.33%, and 6.58% of YFP+ neurons co-expressed nNOS, 5-HT, *vip*, and *slc18a3a*, respectively, indicating the presence of distinct YFP+ neuronal subtypes prior to ablation, which fall into the three major classes of ENS neurons [(Kuil et al., 2023; Li et al., 2025; Uyttebroek et al., 2010), **Figure S7**].

To examine if all YFP+ expressing subtypes regenerated, we analyzed the number of YFP+/subtype+ neurons in the MTZ-treated group at 9 dpt and compared them to untreated control and baseline at 0 dpt control. Notably, the number of YFP+/nNOS+ neurons remained unchanged between 0 control and 9 dpt control, and there was no significant difference between MTZ-treated and control group, suggesting robust stability and regenerative capacity for YFP+/nNOS+ neurons (**Figure 6A, B**). Analysis of YFP+/5-HT+ neurons also revealed no significant difference between 0 dpt control and the 9 dpt control group. However, in the MTZ-treated group, the number of YFP+/5-HT+ neurons at 9 dpt remained significantly lower compared to control, indicating a limited regenerative capacity or delayed regenerative kinetics for this neuronal subtype (**Figure 6C, D**).

418 Using HCR to detect *vip* and *slc18a3a* expression, we found that the number of YFP+/*vip*+
419 neurons significantly decreased within the control group between 0 and 9 dpt. However, no
420 significant difference was observed between the MTZ-treated and control groups at 9 dpt,
421 suggesting that YFP+/*vip*+ neurons had successfully regenerated by this time point (**Figure 6E,**
422 **F)**. Lastly, analysis of the cholinergic marker *slc18a3a* showed no significant differences across
423 groups, indicating that YFP+/*slc18a3a*+ neurons remained stable in the control group and were
424 successfully restored following regeneration (**Figure 6G, H**).

425 Overall, these findings suggest that the majority of YFP+ cells are nitrergic neurons before
426 ablation. After regeneration, YFP+/nNOS+, YFP+/*vip*+ and YFP+/*slc18a3a*+ neurons are
427 successfully restored. In contrast the YFP+/5-HT+ neurons exhibited lower and/or slower
428 regenerative capacity compared to the other subtypes.

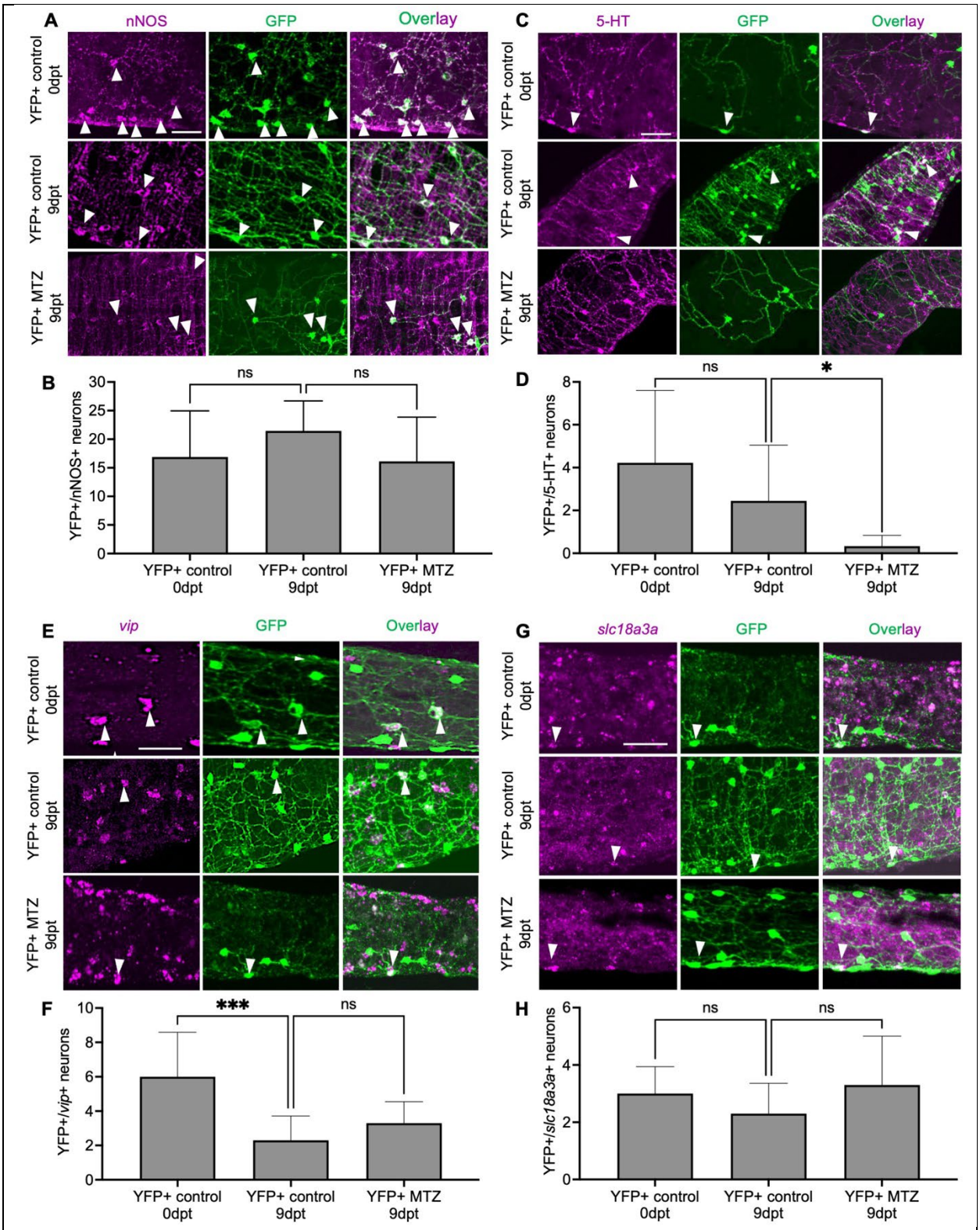

Figure 6: YFP+/nNOS+, YFP+/*vip*+ and YFP+/*slc18a3a*+ but not YFP+/5-HT+ neurons regenerate following ablation.

(A) Example of nNOS+ (magenta) and YFP+ (labeled with anti-GFP antibody, green) neurons that co-localize (overlay) at 0 dpt control (before treatment) and at 9 dpt in YFP+ control and YFP+ MTZ groups (white arrowheads). **(B)** Quantification of GFP+/nNOS+ neurons at 0 dpt control and 9 dpt in YFP+ control and YFP+ MTZ shows no significant difference. **(C)** Example of 5-HT (magenta) and YFP+ (labeled with anti-GFP antibody, green) neurons that co-localize (overlay) at 0 dpt control and 9 dpt in YFP+ control and YFP+ MTZ groups (white arrowheads). **(D)** Quantification of GFP+/5-HT+ at 0 dpt control and 9 dpt in YFP+ control and YFP+ MTZ. There is no significant difference between 0 dpt and 9 dpt in the YFP+ control group, but GFP+/5-HT+ neurons are significantly reduced in in the MTZ-treated group compared to the control group at 9 dpt. (**E)** Example of *vip* (magenta) and YFP+ (labeled with anti-GFP antibody, green) neurons that co-localize (overlay) at 0 dpt control (before treatment), and 9 dpt in YFP+ control and YFP+ MTZ (white arrowheads). **(F)** Quantification of GFP+/*vip*+ neuron at 0 dpt control and 9 dpt in both YFP+ control and YFP+ MTZ groups. A significant difference is observed between 0 dpt and 9 dpt control groups. However, there is no significant difference between 9 dpt control and MTZ-treated groups. **(G)** Example of *slc18a3a* (magenta) and YFP+ (labeled with anti-GFP antibody, green) neurons that co-localize (overlay) at 0 dpt control and 9 dpt of YFP+ control and YFP+ MTZ (white arrowheads). **(H)** Quantification of GFP+/*slc18a3a*+ neurons shows no significant difference between the groups. **(A, C, E, G)** Maximum projection confocal images of dissected intestines at stage indicated. Data are presented as mean ± SD (n = 10 larvae per group, 2 experiments); Statistical significance: ***$p < 0.001$ and *$p < 0.05$; ns = non-significant difference; dpt = days post treatment; Scale bars = 10 µm.

429

430 **Decreased gut wave movements recover to control levels after neuronal regeneration**

431 ENS neurons play a critical role in regulating gut motility. Excitatory motor neurons mediate muscle
432 contractions and inhibitory motor neurons induce muscle relaxation (Furness, 2012; Kunze &
433 Furness, 1999). We find that major portion of YFP+ neurons co-express inhibitory and excitatory
434 motor neurons markers (**Figure S6**). Thus, we aimed to determine i) whether the loss of YFP+
435 neurons affects gut motility and ii) whether the regenerated neurons restore gut function after
436 ablation.

437 To assess this, we examined one measure of gut motility, the time of the Peristaltic Wave Interval
438 (PWI) of anterograde movements (Holmberg et al., 2006). We measured the PWI at three different
439 time points at 1 dpt, 3 dpt and 9 dpt in YFP+ and YFP- MTZ treated fish, and YFP+ untreated

440 controls. We included the YFP- MTZ treated group to determine if MTZ treatment alone impacted
441 PWI. At 1 dpt, we found no significant difference in the PWI time between control and treated groups
442 (**Figure 7A, Supplementary Videos S1-3**). However, at 3 dpt, the PWI time in the YFP+ MTZ
443 treated group increased significantly compared to both control groups, suggesting slower peristaltic
444 movement in the YFP+ MTZ group (**Figure 7B, supplementary videos S4-6**). At 9 dpt, the PWI
445 time in the YFP+ MTZ treated group was back to control levels (**Figure 7C, supplementary videos**
446 **S7-9**). Overall, our results suggest that gut motility function is affected after YFP+ neuronal loss and
447 then restored after regeneration, indicating functional recovery.

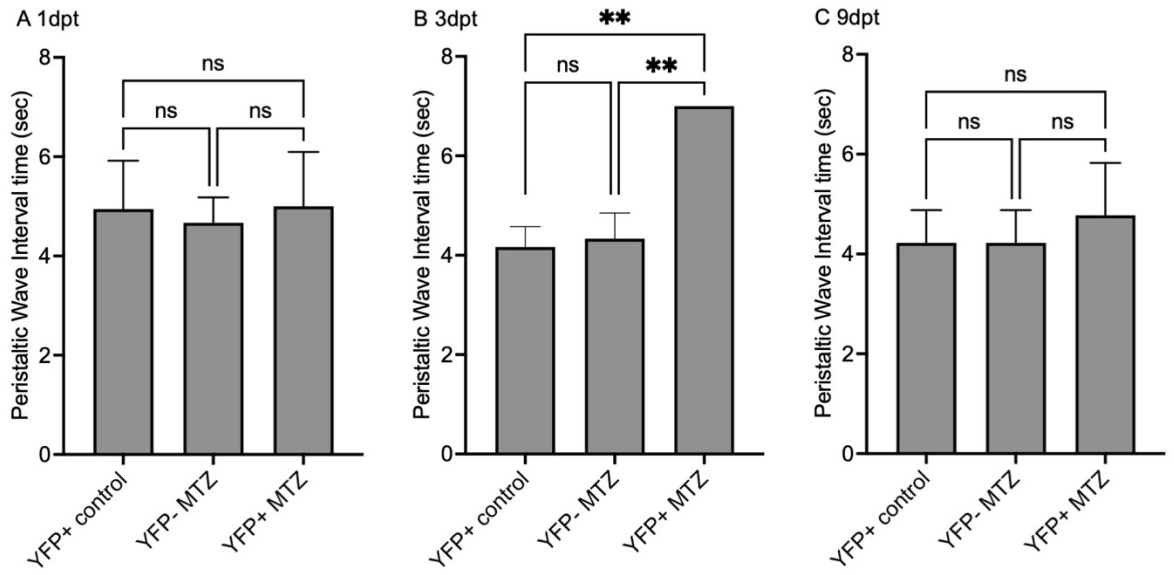

Figure 7. Peristaltic Interval Wave time recovers at 9 dpt after YFP+ neuron ablation. (A) At 1dpt, there is no significant difference in gut PWI time across all experimental groups, YFP+ MTZ treated, YFP+ untreated control, YFP- MTZ treated. **(B)** At 3dpt, YFP+MTZ treated larvae showed significantly slower gut PWI time compared to both control groups. **(C)** At 9dpt, there was no significant difference in PWI across all experimental groups. Data are presented as mean ± SD (n = 6 larvae per group, 2 experiments); Statistical significance: $^{**}p < 0.01$; ns = non-significant; dpt = days post treatment.

448

449 **Discussion**

450 The topic of reparative regeneration has gained significant attention over the past decade due to its
451 potential therapeutic implications, for example to treat ENS diseases with loss of ENS neurons. Yet,
452 to date, no study has demonstrated functional ENS neuron regeneration either in mammalian
453 models or in zebrafish. In the present study, we show targeted chemogenetic ablation and functional

454 regeneration of ENS neurons for the first time in zebrafish (**Figure 8**). Our results determined the
455 spatial and temporal cellular dynamics of targeted neuron ablation as demonstrated by increased
456 TUNEL labeling at 6hpt. Additionally, we observed an acute L-plastin+ immune cell response at 6
457 hpt that resolves within 1 dpt (**Figure 8**). We find full recovery of ablated neuron numbers by 9 dpt
458 for the majority on ENS neuron subtypes investigated. Specifically, among the regenerated neurons,
459 we found full recovery of nitrergic, cholinergic, and VIPergic subtypes, but only partial or delayed
460 regeneration of serotonergic neurons. Importantly, we also showed functional impacts of neuronal
461 ablation on a gut motility parameter and its functional recovery suggesting functional regeneration in
462 our system (**Figure 8**).

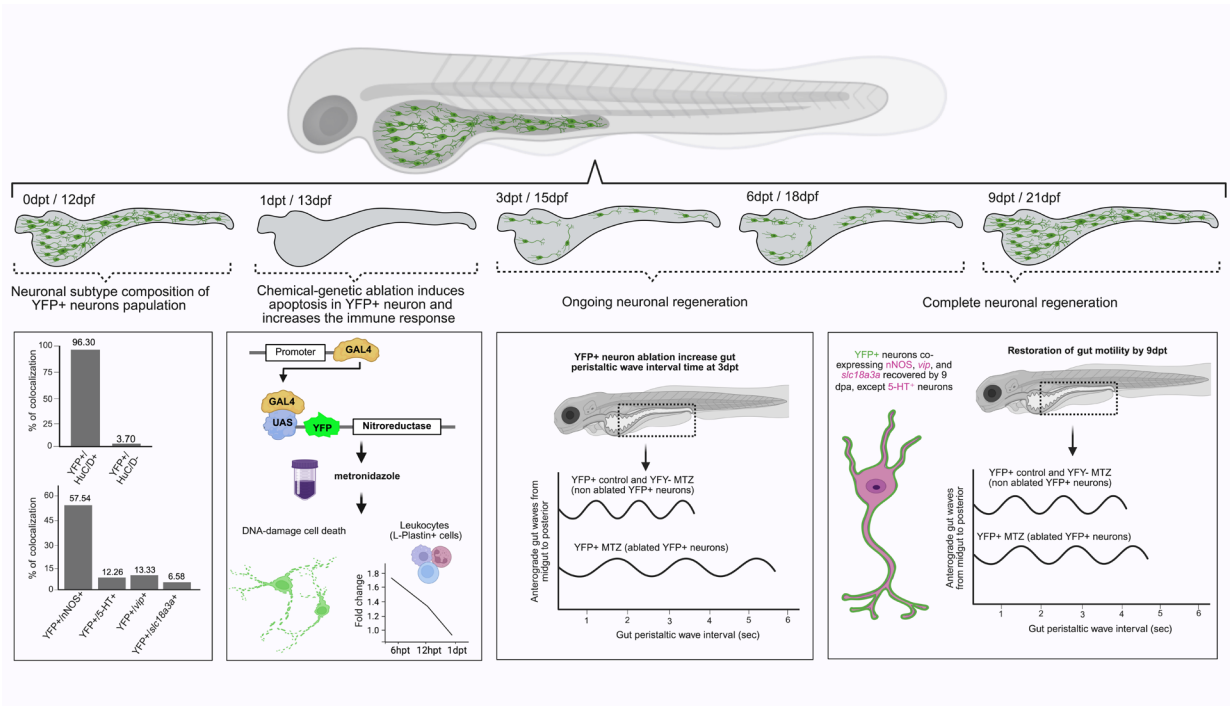

Figure 8. Timeline of events after targeted ablation and regeneration of ENS neurons in zebrafish. Timeline from 0 dpt / 12 dpf to 9 dpt / 21 dpf depicts the different events: i) Neuronal subtype composition of YFP+ neuron population at 0 dpt; ii) Chemogenetic ablation approach activates cell death of YFP+ neurons to completely ablate YFP+ neurons; iii) neuronal regeneration at 3 and 6 dpt which affects gut peristalsis at 3dpt; iv) complete regeneration of YFP+ cells and functional recovery at 9 dpt. **Panel 1** (0dpt / 12dpf): YFP+ cells co-localize with the pan-neuronal marker HuC/D and various neuronal subtypes (nNOS, 5-HT, *vip*, and *slc18a31a*). **Panel 2** (1dpt / 13dpf): Set-up of Gal4-UAS:NTR 2.0 based ablation system. MTZ treatment induces DNA-damage cell death in YFP+ neurons as

confirmed by TUNEL assay at 6hpt. Additionally, there is an acute accumulation of L-plastin+ immune cells at 6hpt that resolves within 24 hours. **Panel 3** (3dpt / 15 dpf): Neuronal ablation resulted in increased peristaltic wave interval time, reflecting reduced gut motility. **Panel 4** (9dpt / 21dpf): Complete recovery of YFP+ neurons and most neuronal subtypes (nNOS+, *vip*+, *slc18a31*+), except 5-HT+ neurons and full functional recovery of gut motility. dpf = days post fertilization, dpt = days post treatment.

Extensive ENS neuron ablation and their complete regeneration in zebrafish

In zebrafish, the only two studies to study ENS neurons regeneration used focal laser ablation to target a few ENS neurons in a small gut region. Both studies reported generation of new neurons following ablation (El-Nachef & Bronner, 2020, Ohno et al., 2021). However, quantification of regenerated neurons showed that they did not return to control levels in the analyzed time frame, nor were impacts on gut function investigated (Ohno et al., 2021). In our study, using chemogenetic ablation of ~44.4 ENS neurons, we find robust regeneration of ablated cells to control levels by 9 dpt which stay at control levels through 15 dpt, the last time point that we analyzed. We find that different neuronal subtypes within the three main ENS neuron classes are able to regenerate but identify interesting subtype-specific differences in regenerative capacity or timing (**Figure 8**). Our work also shows for the first time recovery of a parameter of gut function - gut wave propagation - indicative of successful functional regeneration (**Figure 8**). In addition, our approach has several experimental advantages compared to laser ablation. First, laser ablation is less efficient, as it can only ablate a limited number of neurons within specific gut regions (El-Nachef & Bronner, 2020, Ohno et al., 2021). For instance, one study only ablated ~16 neurons within one-somite-width of the posterior gut at 10-15 dpf (Ohno et al., 2021). In contrast, our chemogenetic ablation system successfully ablated on average 44 neurons throughout the whole gut, significantly improving efficiency. Second, laser ablation is time-consuming as it requires individual larval preparation and precise manual targeting (Ohno et al., 2021). In contrast, our methods enable the simultaneous ablation of ENS neurons in several hundred of larvae. Third, laser irradiation can cause unintended damage to non-neuronal, surrounding tissues, including smooth muscle and epithelial cells, which may impact regeneration and complicate downstream analyses such as gut motility. In contrast, our approach is spatiotemporally controlled ablation that precisely targets only specific ENS neurons and had no deleterious effects on the overall neuronal population in the gut (**Figure 8**).

490 **Zebrafish are a powerful model system to study ENS regeneration**

491 So far, ENS regeneration research has mostly focused on mammalian model systems with only
492 limited work in non-mammalian models such as zebrafish (Corvetti et al., 2001; El-Nachef &
493 Bronner, 2020; Gabella & Trigg, 1984; Galligan et al., 1989; Hanani et al., 2003; Jew et al., 1989;
494 Joseph et al., 2011; Karaosmanoğlu et al., 1996; Laranjeira et al., 2011; Luck et al., 1993; Ohno et
495 al., 2021; Stavely et al., 2024; Tokui et al., 1994). Previous studies in mammalian models involving
496 surgical (Galligan et al., 1989; Karaosmanoğlu et al., 1996; Tokui et al., 1994), stenosis (Corvetti et
497 al., 2001; Gabella & Trigg, 1984; Jew et al., 1989; Joseph et al., 2011), and chemical (Hanani et al.,
498 2003; Laranjeira et al., 2011; Luck et al., 1993) ablation methods consistently report incomplete
499 neuronal regeneration, and gut region- or species-specific differences in regenerative outcomes of
500 ENS neurons (Rueckert and Ganz, 2022). Notably, all previous approaches also reported structural
501 abnormalities at the injury site by co-lateral damage of surrounding tissues. To address this, recent
502 works in adult mice reported focal ablation specifically of ENS neurons using a diphtheria toxin-
503 based chemogenetic ablation approach (Bhave et al., 2019; Stavely et al., 2024). Even though this
504 study reported that mature, post-mitotic enteric neurons in adult mice can regenerate axons and
505 reinnervate the gut after injury, there was still limited regeneration of neurons even three months
506 after ablation (Stavely et al., 2024). This indicates that mammals have generally limited ENS
507 regenerative abilities. In contrast, the present study demonstrates that zebrafish are a powerful
508 model to study the signals and cellular-molecular processes underlying functional ENS regeneration.
509 Our spatio-temporally controlled approach ablates approximately one fifth of all ENS neurons by
510 inducing cell death with subsequent full recovery after only 9 days. Ablation along the entire gut will
511 enable the analysis of cellular responses and gene regulatory programs active during ENS
512 regeneration as whole guts can be analyzed. We find an acute immune response during the time of
513 cell death which normalizes at 1 dpt. Studies on adult zebrafish brain traumatic injury and selective
514 rod photoreceptor ablation in the retina have demonstrated that immune responses are crucial
515 components of regenerative processes (Kyritsis et al., 2012; White et al., 2017). In our study,
516 selective ablation of enteric neurons (**Figure 8**) led to a marked accumulation of L-plastin+ cells as
517 early as 6 hours after MTZ treatment. Given that L-plastin is strongly expressed in leukocytes,
518 including macrophages, monocytes, and neutrophils (Hiroto Shinomiya, 2012), this finding suggests
519 that selective neuronal death in the ENS triggers an acute immune cell recruitment, similar to what
520 has been described in models of traumatic brain injury and retinal regeneration (Kyritsis et al., 2012;
521 White et al., 2017). Future studies will be needed to provide mechanistic insights into how immune–
522 neural interactions (Graves et al., 2021) regulate ENS regeneration. Our approach thus provides a

523 rapid experimental setup to identify the signals and cellular responses important for neuronal
524 regeneration in the ENS in the future (**Figure 8**).

525 **Regeneration of neurons in the zebrafish CNS *vs* ENS**

526 The zebrafish central nervous system has been extensively studied with regards to its regenerative
527 capacity (Kaslin et al., 2009, 2013; März et al., 2010) while little is known about ENS regeneration
528 (Ohno et al., 2021). In the central nervous system, brain regions show different capacities to
529 regenerate neuronal subtypes. In the zebrafish telencephalon, all ablated neuron types regenerate
530 (Barbosa et al., 2015; Kroehne et al., 2011; Reimer et al., 2008), whereas the cerebellum is capable
531 of regenerating many, but not all neuron types (Kaslin et al., 2017). This variable regenerative
532 capacity of the cerebellum has been attributed to varying ability of cerebellar stem and progenitor
533 cells to generate neurons and glia throughout the lifespan (Kaslin et al., 2009, 2013). We also find
534 differences in regeneration of neuron types in the ENS where some subtypes (nitrergic, cholinergic
535 and VIPergic) regenerate fully, whereas serotonergic neurons do not reach control levels (**Figure 8**).
536 There could be three possibilities for this difference in regeneration: (1) serotonergic neurons take
537 longer to regenerate, (2) the progenitor cells or cellular mechanisms to regenerate serotonergic
538 neurons are not activated at this stage of post-embryonic development, and (3) the low level of
539 serotonergic cell loss incurred is insufficient to trigger serotonergic cell replacement. Further work
540 will determine which cellular responses are triggered after cell ablation and the progenitor
541 population(s) that generate new ENS neurons and neuronal subtypes in zebrafish.

542

543 **Supplementary Materials**
544 The following supporting information can be downloaded at: https:
545

546 **Author Contributions**
547 Conceptualization: M.A.S, K.M., H.R., J.G. Methodology, Data curation, Validation, Formal
548 Analysis and Investigation: M.A.S, K.M., H.R. Visualization: M.A.S. Writing—Original Draft
549 Preparation: M.A.S. Writing—Review and Editing: M.A.S, K.M., H.R., A.V.S., D.F.A., J.S.M., and
550 J.G. Supervision, Project Administration, Funding Acquisition and Recourses: D.F.A., J.S.M.,
551 J.G. All authors have read and agreed to the published version of the manuscript.
552
553
554
555

Funding:

This work was supported by NSF CAREER #2143267 to J.G., NIH R21NS123629 to J.G., and a Research Grant from the American Neurogastroenterology and Motility Society to J.G. NIH R01OD020376 to J.S.M. and D.F.A., supported development of the improved NTR 2.0 enzyme.

Institutional Review Board Statement:

The animal study protocol was approved by the Michigan State University Institutional Animal Care and Use Committee.

Acknowledgments

We want to thank Rachel Alcorn, Taylor Lawrence, Giovanna Haddock, Kristen Lounsbury, Anthony Turner, Samantha Lampman, and Sharon An for excellent fish care.

Conflicts of Interest

The authors declare no competing or financial interests

List of Abbreviations

ENS = Enteric nervous system
MTZ = Metronidazole
HSCR = Hirschsprung Disease
DPF = Days post fertilization
DPT = Days post treatment
HPT = Hours post treatment
NTR = Nitroreductase
YFP = Yellow fluorescent protein
GFP = Green fluorescent protein
UAS = Upstream activating sequence
PWI = Peristaltic Wave Interval
TdT = Terminal deoxynucleotidyl Transferase
BSA = Bovin serum albumin
PBS = Phosphate-Buffered Saline
HCR = Hybridization Chain Reaction
SD = standard deviation

590 **References**

591 Ariga, J., Walker, S. L., & Mumm, J. S. (2010). Multicolor time-lapse imaging of
592 transgenic zebrafish: Visualizing retinal stem cells activated by targeted neuronal
593 cell ablation. *Journal of Visualized Experiments*, *43*.
594 https://doi.org/https://doi.org/10.3791/2093
595 Asakawa, K., Suster, M. L., Mizusawa, K., Nagayoshi, S., Kotani, T., Urasaki, A.,
596 Kishimoto, Y., Hibi, M., & Kawakami, K. (2008). Genetic dissection of neural circuits
597 by Tol2 transposon-mediated Gal4 gene and enhancer trapping in zebrafish.
598 *Proceedings of the National Academy of Sciences of the United States of America*,
599 *105*(4), 1255–1260. https://doi.org/10.1073/pnas.0704963105
600 Bandla, A., Melancon, E., Taylor, C. R., Davidson, A. E., Eisen, J. S., & Ganz, J. (2022).
601 A New Transgenic Tool to Study the Ret Signaling Pathway in the Enteric Nervous
602 System. *International Journal of Molecular Sciences*, *23*(24), 15667.
603 https://doi.org/10.3390/ijms232415667
604 Barbosa, J. S., Sanchez-Gonzalez, R., Di Giaimo, R., Baumgart, E. V., Theis, F. J.,
605 Götz, M., & Ninkovic, J. (2015). Live imaging of adult neural stem cell behavior in
606 the intact and injured zebrafish brain. *Science*, *348*(6236), 789–793.
607 https://doi.org/10.1126/science.aaa2729
608 Bhave, S., Arciero, E., Baker, C., Ho, W. L., Stavely, R., Goldstein, A. M., & Hotta, R.
609 (2019). Enteric neuronal cell therapy reverses architectural changes in a novel
610 diphtheria toxin-mediated model of colonic aganglionosis. *Scientific Reports*, *9*(1),
611 1–12. https://doi.org/10.1038/s41598-019-55128-4
612 Burns, A. J., Goldstein, A. M., Newgreen, D. F., Stamp, L., Metzger, M., Hotta, R.,
613 Young, H. M., Andrews, P. W., Belkind-gerson, J., Bondurand, N., Bornstein, J. C.,
614 Yee, W., Cheah, K., Gershon, M. D., Heuckeroth, R. O., Robert, M. W., Just, L.,
615 Kapur, R. P., King, S. K., … Urology, P. (2016). *White paper on guidelines*
616 *concerning enteric nervous system stem cell therapy for enteric neuropathies⋆*.
617 *417*(2), 229–251. https://doi.org/10.1016/j.ydbio.2016.04.001
618 Butler Tjaden, N. E., & Trainor, P. A. (2013). The developmental etiology and
619 pathogenesis of Hirschsprung disease. *Translational Research*, *162*(1), 1–15.
620 https://doi.org/10.1016/j.trsl.2013.03.001
621 Cao, J., & Poss, K. D. (2018). The epicardium as a hub for heart regeneration. *Nature*
622 *Reviews Cardiology*, *15*(10), 631–647. https://doi.org/10.1038/s41569-018-0046-4
623 Corvetti, G., Fornaro, M., Geuna, S., Poncino, A., & Giacobini-Robecchi, M. G. (2001).
624 Unscheduled DNA synthesis in rat adult myenteric neurons: An
625 immunohistochemical study. *NeuroReport*, *12*(10), 2165–2168.
626 https://doi.org/10.1097/00001756-200107200-00024
627 Cusack, C. L., Swahari, V., Henley, W. H., Ramsey, J. M., & Deshmukh, M. (2013).
628 Distinct Pathways Mediate Axon Degeneration during Apoptosis and Axon-Specific
629 Pruning. *Nature Communications*, *4*(1876). https://doi.org/doi:
630 10.1038/ncomms2910
631 Davison, J. M., Akitake, C. M., Goll, M. G., Rhee, J. M., Gosse, N., Baier, H., Halpern,
632 M. E., Leach, S. D., & Parsons, M. J. (2007). Transactivation from Gal4-VP16
633 transgenic insertions for tissue-specific cell labeling and ablation in zebrafish.
634 *Developmental Biology*, *304*(2), 811–824.
635 https://doi.org/10.1016/j.ydbio.2007.01.033

Diep, C. Q., Ma, D., Deo, R. C., Holm, T. M., Naylor, R. W., Arora, N., Wingert, R. A., Bollig, F., Djordjevic, G., Lichman, B., Zhu, H., Ikenaga, T., Ono, F., Englert, C., Cowan, C. A., Hukriede, N. A., Handin, R. I., & Davidson, A. J. (2011). Identification of adult nephron progenitors capable of kidney regeneration in zebrafish. *Nature*, *470*, 95–101. https://doi.org/10.1038/nature09669

El-Nachef, W. N., & Bronner, M. E. (2020). De novo enteric neurogenesis in post-embryonic zebrafish from Schwann cell precursors rather than resident cell types. *Development (Cambridge)*, *147*(13). https://doi.org/10.1242/dev.186619

Furness, J. B. (2012). The enteric nervous system and neurogastroenterology. *Nature Reviews Gastroenterology and Hepatology*, *9*(5), 286–294. https://doi.org/10.1038/nrgastro.2012.32

Gabella, G., & Trigg, P. (1984). Size of neurons and glial cells in the enteric ganglia of mice, guinea-pigs, rabbits and sheep. *Journal of Neurocytology*, *13*(1), 49–71. https://doi.org/10.1007/BF01148318

Galligan, J. J., Furness, J. B., & Costa, M. (1989). Migration of the myoelectric complex after interruption of the myenteric plexus: Intestinal transection and regeneration of enteric nerves in the guinea pig. *Gastroenterology*, *97*(5), 1135–1146. https://doi.org/10.1016/0016-5085(89)91683-1

Ganz, J. (2018). Gut feelings: Studying enteric nervous system development, function, and disease in the zebrafish model system. *Developmental Dynamics*, *247*(2), 268–278. https://doi.org/10.1002/dvdy.24597

Graves, C. L., Chen, A., Kwon, V., & Shiau, C. E. (2021). Zebrafish harbor diverse intestinal macrophage populations including a subset intimately associated with enteric neural processes. *IScience*, *24*(6), 102496. https://doi.org/10.1016/j.isci.2021.102496

Ham, T. J., Mapes, J., Kokel, D., & Peterson, R. T. (2010). Live imaging of apoptotic cells in zebrafish. *The FASEB Journal*, *24*(11), 4336–4342. https://doi.org/10.1096/fj.10-161018

Hanani, M., Ledder, O., Yutkin, V., Abu-Dalu, R., Huang, T. Y., Härtig, W., Vannucchi, M. G., & Faussone-Pellegrini, M. S. (2003). Regeneration of myenteric plexus in the mouse colon after experimental denervation with benzalkonium chloride. *Journal of Comparative Neurology*, *462*(3), 315–327. https://doi.org/10.1002/cne.10721

Hanovice, N. J., Leach, L. L., Slater, K., Gabriel, A. E., Romanovicz, D., Shao, E., Collery, R., Burton, E. A., Lathrop, K. L., Link, B. A., & Gross, J. M. (2019). Regeneration of the zebrafish retinal pigment epithelium after widespread genetic ablation. In *PLoS Genetics* (Vol. 15, Issue 1). https://doi.org/10.1371/journal.pgen.1007939

Hao, M. M., & Young, H. M. (2009). Development of enteric neuron diversity. *Journal of Cellular and Molecular Medicine*, *13*(7), 1193–1210. https://doi.org/10.1111/j.1582-4934.2009.00813.x

Heanue, T. A., Boesmans, W., Bell, D. M., Kawakami, K., Berghe, P. Vanden, & Pachnis, V. (2016). *A Novel Zebrafish ret Heterozygous Model of Hirschsprung Disease Identifies a Functional Role for mapk10 as a Modifier of Enteric Nervous System Phenotype Severity*. *12*(11), 1–23. https://doi.org/doi:10.1371/journal.pgen.1006439

Hiroto Shinomiya. (2012). Plastin Family of Actin-Bundling Proteins: Its Functions in Leukocytes, Neurons, Intestines, and Cancer. *Nternational Journal of Cell Biology*, *11*(1), 1–8. https://doi.org/10.1155/2012/213492

Holmberg, A., Olsson, C., & Holmgren, S. (2006). The effects of endogenous and exogenous nitric oxide on gut motility in zebrafish Danio rerio embryos and larvae. *Journal of Experimental Biology*, *209*(13), 2472–2479. https://doi.org/10.1242/jeb.02272

Howe, K., Clark, M. D., Torroja, C. F., Torrance, J., Berthelot, C., & Muffato, M. (2013). The zebrafish reference genome sequence and its relationship to the human genome. *Nature*, *496*(7446), 598–503. https://doi.org/10.1038/nature12111.The

Ibarra-García-Padilla, R., Howard, A. G. A., Singleton, E. W., & Uribe, R. A. (2021). A protocol for whole-mount immuno-coupled hybridization chain reaction (WICHCR) in zebrafish embryos and larvae. *STAR Protocols*, *2*(3). https://doi.org/10.1016/j.xpro.2021.100709

Jew, J. Y., Zhang, M. Q., Williams, T. H., & Gabella, G. (1989). The Intestine as a Model for Neuronal Plasticity. *Archives of Histology and Cytology*, *52*(Suppl.), 167–180. https://doi.org/10.1679/aohc.52.Suppl_167

Jianlong Li, Prochaska, M., Maney, L., & Wallace, K. N. (2020). Development and organization of the zebrafish intestinal epithelial stem cell niche. *Development Dynamics*, *249*(1), 76–87.

Joseph, N. M., He, S., Quintana, E., Kim, Y. G., Núñez, G., & Morrison, S. J. (2011). Enteric glia are multipotent in culture but primarily form glia in the adult rodent gut. *Journal of Clinical Investigation*, *121*(9), 3398–3411. https://doi.org/10.1172/JCI58186

Karaosmanoğlu, T., Müftüoğlu, S., Dağdeviren, A., Durgun, B., Aygün, B., & Örs, Ü. (1996). Morphological changes in the myenteric plexus of rat ileum after transection and end-to-end anastomosis. *Journal of Anatomy*, *188*(2), 323–331.

Kaslin, J., Ganz, J., Geffarth, M., Grandel, H., Hans, S., & Brand, M. (2009). Stem cells in the adult zebrafish cerebellum: Initiation and maintenance of a novel stem cell niche. *Journal of Neuroscience*, *29*(19), 6142–6153. https://doi.org/10.1523/JNEUROSCI.0072-09.2009

Kaslin, J., Kroehne, V., Benato, F., Argenton, F., & Brand, M. (2013). Development and specification of cerebellar stem and progenitor cells in zebrafish: From embryo to adult. *Neural Development*, *8*(1). https://doi.org/10.1186/1749-8104-8-9

Kaslin, J., Kroehne, V., Ganz, J., Hans, S., Brand, M., Kaslin, J., Kroehne, V., Ganz, J., Hans, S., & Brand, M. (2017). Correction to: Distinct roles of neuroepithelial-like and radial glia-like progenitor cells in cerebellar regeneration (Development (Cambridge), (2017) 144, (1462-1471), 10.1242/dev.144907). *Development (Cambridge)*, *144*(18), 3388. https://doi.org/10.1242/dev.158600

Kawakami, K., Abe, G., Asada, T., Asakawa, K., Fukuda, R., Ito, A., Lal, P., Mouri, N., Muto, A., Suster, M. L., Takakubo, H., Urasaki, A., Wada, H., & Yoshida, M. (2010). ZTrap: Zebrafish gene trap and enhancer trap database. *BMC Developmental Biology*, *10*. https://doi.org/10.1186/1471-213X-10-105

Kimmel, C. B., Ballard, W. W., Kimmel, S. R., & F., B. U. homas. (1995). Stages of embryonic development of the zebrafish. *Developmental Dynamics*, *203*, 253–310. https://doi.org/https://doi.org/10.1002/aja.1002030302

Kizil, C., Kaslin, J., Kroehne, V., & Brand, M. (2012). Adult neurogenesis and brain regeneration in zebrafish. *Developmental Neurobiology*, *72*(3), 429–461. https://doi.org/10.1002/dneu.20918

Kroehne, V., Freudenreich, D., Hans, S., Kaslin, J., & Brand, M. (2011). Regeneration of the adult zebrafish brain from neurogenic radial glia-type progenitors. *Development*, *138*(22), 4831–4841. https://doi.org/10.1242/dev.072587

Kuil, L. E., Chauhan, R. K., Cheng, W. W., Hofstra, R. M. W., & Alves, M. M. (2021). Zebrafish: A Model Organism for Studying Enteric Nervous System Development and Disease. *Frontiers in Cell and Developmental Biology*, *8*(January), 1–15. https://doi.org/10.3389/fcell.2020.629073

Kuil, L. E., Kakiailatu, N. J. M., Windster, J. D., Bindels, E., Zink, J. T. M., van der Zee, G., Hofstra, R. M. W., Shepherd, I. T., Melotte, V., & Alves, M. M. (2023). Unbiased characterization of the larval zebrafish enteric nervous system at a single cell transcriptomic level. *IScience*, *26*(7), 107070. https://doi.org/10.1016/j.isci.2023.107070

Kulkarni, A. A., Conteh, A. M., Sorrell, C. A., Mirmira, A., Tersey, S. A., Mirmira, R. G., Linnemann, A. K., & Anderson, R. M. (2018). An in vivo zebrafish model for interrogating ROS-mediated pancreatic β-cell injury, response, and prevention. *Oxidative Medicine and Cellular Longevity*, 1–8. https://doi.org/10.1155/2018/1324739

Kunze, W. A. A., & Furness, J. B. (1999). The enteric nervous system and regulation of intestinal motility. *Annual Review of Physiology*, *61*, 117–142. https://doi.org/10.1146/annurev.physiol.61.1.117

Kyritsis, N., Kizil, C., Zocher, S., Kroehne, V., Kaslin, J., Freudenreich, D., Iltzsche, A., & Brand, M. (2012). Acute inflammation initiates the regenerative response in the adult zebrafish brain. *Science*, *338*(6112), 1353–1356. https://doi.org/10.1126/science.1228773

Laranjeira, C., Sandgren, K., Kessaris, N., Richardson, W., Potocnik, A., Vanden Berghe, P., & Pachnis, V. (2011). Glial cells in the mouse enteric nervous system can undergo neurogenesis in response to injury. *Journal of Clinical Investigation*, *121*(9), 3412–3424. https://doi.org/10.1172/JCI58200

Lee, E., Song, C. H., Bae, S. J., Ha, K. T., & Karki, R. (2023). Regulated cell death pathways and their roles in homeostasis, infection, inflammation, and tumorigenesis. *Experimental and Molecular Medicine*, *55*(8), 1632–1643. https://doi.org/10.1038/s12276-023-01069-y

Li, C., Gehring, J., & Bronner, M. E. (2025). Spatiotemporal dynamics of the developing zebrafish enteric nervous system at the whole-organ level. *Developmental Cell*, *60*(4), 613-629.e6. https://doi.org/10.1016/j.devcel.2024.11.006

Luck, M. S., Dahl, J. L., Boyeson, M. G., & Bass, P. (1993). Neuroplasticity in the smooth muscle of the myenterically and extrinsically denervated rat jejunum. *Cell and Tissue Research*, *271*(2), 363–374. https://doi.org/10.1007/BF00318623

März, M., Chapouton, P., Diotel, N., Vaillant, C., Birgit Hesl, M. T., Lam, C. S., Kah, O., Bally-Cuif, L., & Strähle, U. (2010). Heterogeneity in Progenitor Cell Subtypes in the Ventricular Zone of the Zebrafish Adult Telencephalon. *Glia*, *58*(7), 870–888. https://doi.org/10.1002/glia.20971.

773 Medico, E., Gambarotta, G., Gentile, A., Comoglio, P. M., & Soriano, P. (2001). A gene
774 trap vector system for identifying transcriptionally responsive genes. *Nature*
775 *Biotechnology*, *19*(6), 579–582. https://doi.org/10.1038/89343
776 Niesler, B., Kuerten, S., Demir, I. E., & Schäfer, K. H. (2021). Disorders of the enteric
777 nervous system — a holistic view. *Nature Reviews Gastroenterology and*
778 *Hepatology*, *18*(6), 393–410. https://doi.org/10.1038/s41575-020-00385-2
779 Ohno, M., Nikaido, M., Horiuchi, N., Kawakami, K., & Hatta, K. (2021). The enteric
780 nervous system in zebrafish larvae can regenerate via migration into the ablated
781 area and proliferation of neural crest-derived cells. *Development*, *148*(2).
782 https://doi.org/10.1242/dev.195339
783 Olden, T., Akhtar, T., Beckman, S. A., & Wallace, K. N. (2008). Differentiation of the
784 Zebrafish Enteric Nervous System and Intestinal Smooth Muscle. *Genesis*, *46*(9),
785 484–498. https://doi.org/10.1002/dvg.20429.
786 Reimer, M. M., Sörensen, I., Kuscha, V., Frank, R. E., Liu, C., Becker, C. G., & Becker,
787 T. (2008). Motor neuron regeneration in adult zebrafish. *Journal of Neuroscience*,
788 *28*(34), 8510–8516. https://doi.org/10.1523/JNEUROSCI.1189-08.2008
789 Roach, G., Heath Wallace, R., Cameron, A., Emrah Ozel, R., Hongay, C. F., Baral, R.,
790 Andreescu, S., & Wallace, K. N. (2013). Loss of ascl1a prevents secretory cell
791 differentiation within the zebrafish intestinal epithelium resulting in a loss of distal
792 intestinal motility. *Developmental Biology*, *376*(2), 171–186.
793 https://doi.org/10.1016/j.ydbio.2013.01.013
794 Romero, M. M. G., McCathie, G., Jankun, P., & Roehl, H. H. (2018). Damage-induced
795 reactive oxygen species enable zebrafish tail regeneration by repositioning of
796 Hedgehog expressing cells. *Nature Communications*, *9*(1).
797 https://doi.org/10.1038/s41467-018-06460-2
798 Roy-Carson, S., Natukunda, K., Chou, H. chao, Pal, N., Farris, C., Schneider, S. Q., &
799 Kuhlman, J. A. (2017). Defining the transcriptomic landscape of the developing
800 enteric nervous system and its cellular environment. *BMC Genomics*, *18*(1), 1–24.
801 https://doi.org/10.1186/s12864-017-3653-2
802 Rueckert, H., & Ganz, J. (2022). How to Heal the Gut's Brain: Regeneration of the
803 Enteric Nervous System. *International Journal of Molecular Sciences*, *23*(9).
804 https://doi.org/10.3390/ijms23094799
805 Sharrock, A. V., Mulligan, T. S., Hall, K. R., Williams, E. M., White, D. T., Zhang, L.,
806 Emmerich, K., Matthews, F., Nimmagadda, S., Washington, S., Le, K. D., Meir-
807 Levi, D., Cox, O. L., Saxena, M. T., Calof, A. L., Lopez-Burks, M. E., Lander, A. D.,
808 Ding, D., Ji, H., … Mumm, J. S. (2022). NTR 2.0: a rationally engineered prodrug-
809 converting enzyme with substantially enhanced efficacy for targeted cell ablation.
810 *Nature Methods*, *19*(2), 205–215. https://doi.org/10.1038/s41592-021-01364-4
811 Soret, R., Schneider, S., Bernas, G., Christophers, B., Souchkova, O., Charrier, B.,
812 Righini-Grunder, F., Aspirot, A., Landry, M., Kembel, S. W., Faure, C., Heuckeroth,
813 R. O., & Pilon, N. (2020). Glial Cell-Derived Neurotrophic Factor Induces Enteric
814 Neurogenesis and Improves Colon Structure and Function in Mouse Models of
815 Hirschsprung Disease. *Gastroenterology*, *159*(5), 1824-1838.e17.
816 https://doi.org/10.1053/j.gastro.2020.07.018
817 Stavely, R., Rahman, A. A., Mueller, J. L., Leavitt, A. R., Han, C. Y., Pan, W., Kaiser, K.
818 N., Ott, L. C., Ohkura, T., Guyer, R. A., Burns, A. J., Koppes, A. N., Hotta, R., &

Goldstein, A. M. (2024). Mature enteric neurons have the capacity to reinnervate the intestine with glial cells as their guide. *Neuron*, *112*(18), 3143-3160.e6. https://doi.org/10.1016/j.neuron.2024.06.018

Taylor, C. R., Montagne, W. A., Eisen, J. S., & Ganz, J. (2016). Molecular fingerprinting delineates progenitor populations in the developing zebrafish enteric nervous system. *Developmental Dynamics*, *245*(11), 1081–1096. https://doi.org/10.1002/dvdy.24438

Tokui, K., Sakanaka, M., & Kimura, S. (1994). Progressive reorganization of the myenteric plexus during one year following reanastomosis of the ileum of the guinea pig. *Cell & Tissue Research*, *277*(2), 259–272. https://doi.org/10.1007/BF00327773

Uyttebroek, L., Shepherd, I. T., Harrisson, F., Hubens, G., Blust, R., Timmermans, J.-P., & Nassauw, L. Van. (2010). Neurochemical Coding of Enteric Neurons in Adult and Embryonic Zebrafish (Danio rerio). *J Comp Neuro*, *518*(21), 4419–4438. https://doi.org/10.1002/cne.22464.Neurochemical

Wallace, K. N., Akhter, S., Smith, E. M., Lorent, K., & Pack, M. (2005). Intestinal growth and differentiation in zebrafish. *Mechanisms of Development*, *122*(2), 157–173. https://doi.org/10.1016/j.mod.2004.10.009

Webb, J. F., Shirey, J. E., Desvignes, T., Carey, A., Postlethwait, J. H., Kimmel, S. R., & Ullmann, B. (2009). *Normal table of postembryonic zebra!sh development: Staging by externally visible anatomy of the living fish*. *238*(12), 2975–3015. https://doi.org/10.1002/dvdy.22113

Westerfield, M. (2000). *A Guide for the Laboratory Use of Zebrafish Danio (Brachydanio) rerio* (4th, Ed.). Institute of Neuroscience, University of Oregon, Eugene. Published by the University of Oregon Press.

White, D. T., & Mumm, J. S. (2013). The nitroreductase system of inducible targeted ablation facilitates cell-specific regenerative studies in zebrafish. *Methods*, *62*(3), 232–240. https://doi.org/10.1016/j.ymeth.2013.03.017

White, D. T., Sengupta, S., Saxena, M. T., Xu, Q., Hanes, J., Ding, D., Ji, H., & Mumm, J. S. (2017). Immunomodulation-accelerated neuronal regeneration following selective rod photoreceptor cell ablation in the zebrafish retina. *Proceedings of the National Academy of Sciences of the United States of America*, *114*(18), E3719–E3728. https://doi.org/10.1073/pnas.1617721114

Zhang, Y., Ouyang, J., Qie, J., Zhang, G., Liu, L., & Yang, P. (2019). Optimization of the Gal4/UAS transgenic tools in zebrafish. *Applied Microbiology and Biotechnology*, *103*(4), 1789–1799. https://doi.org/10.1007/s00253-018-09591-0

863 **Supplementary figures**

864

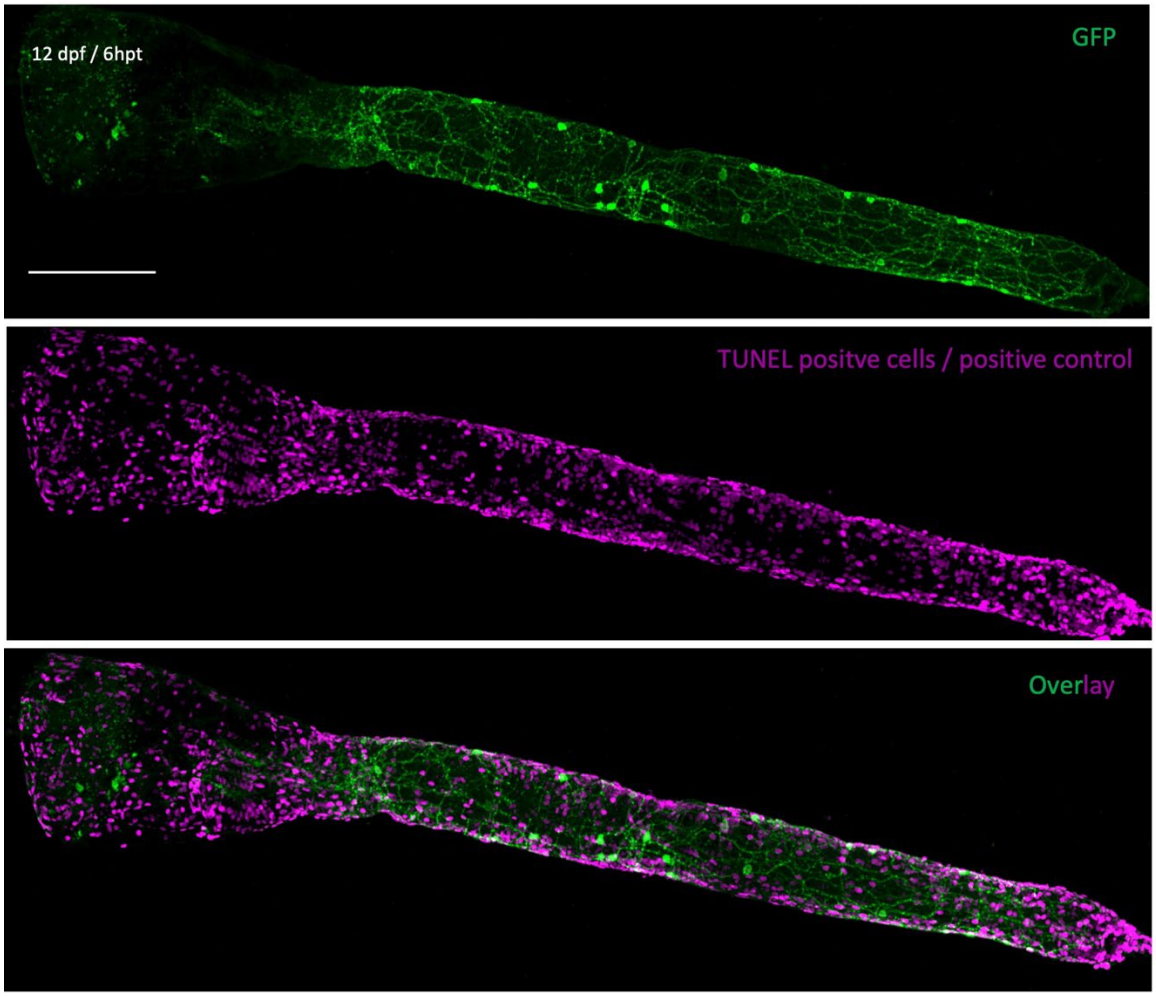

Figure S1: Inducing cell death shows an expected increase in TUNEL+ cells. Inducing cell death as a positive control results in a high number of TUNEL-positive cells (magenta, middle panel) in YFP+ control (green) larvae at 6 hpt (n= 9 larvae, 2 experiments). Maximum projection confocal images of dissected intestine at stage indicated. Scale bar = 100 μm; hpt = hours post treatment.

865

866

867

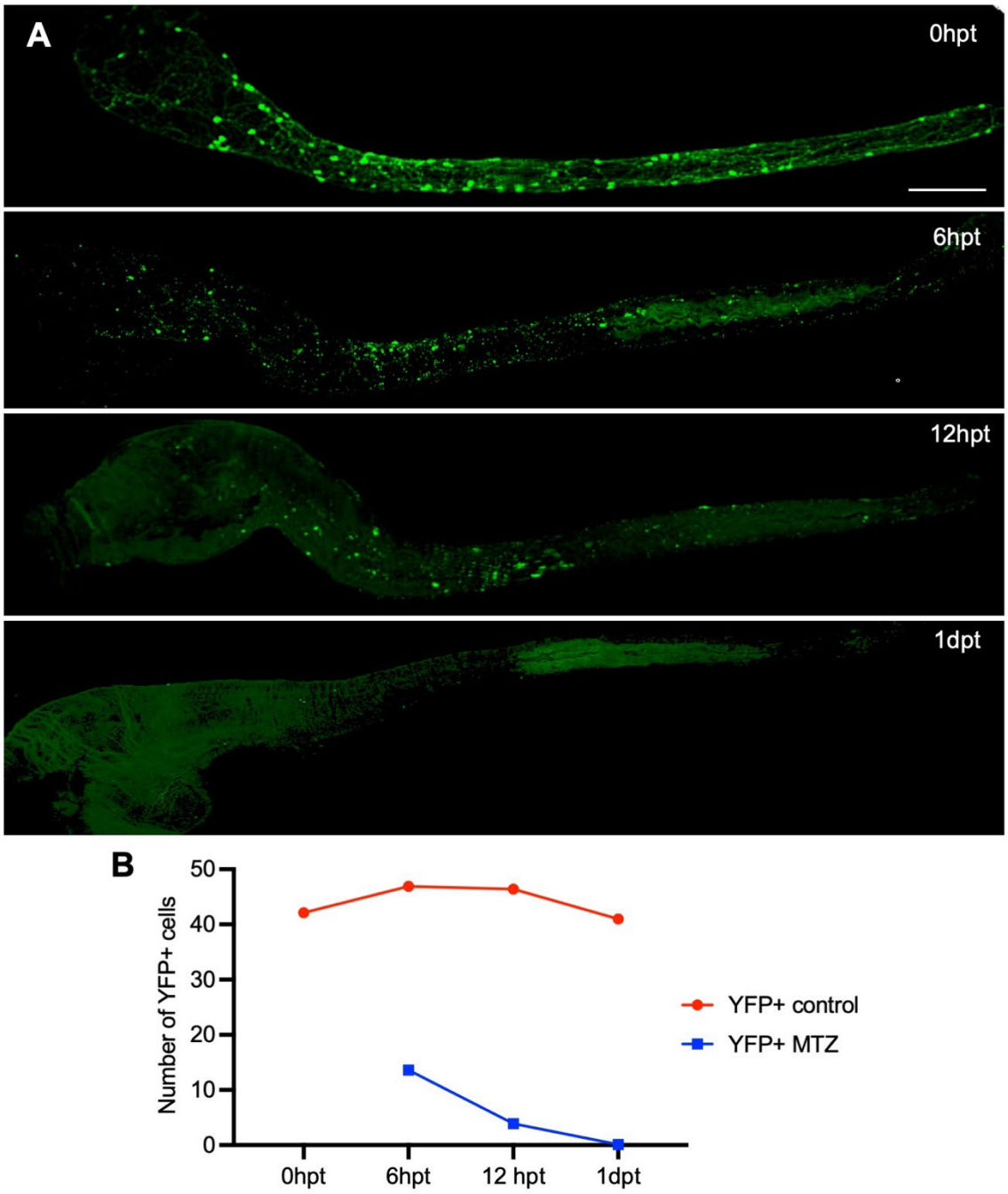

Figure S2. Metronidazole (MTZ)-induced ablation of YFP+ neurons is completed within 24 hours post-treatment. (A) YFP+ neurons (labeled with anti-GFP, green) are present at 0 dpt (before treatment of MTZ), but YFP+ neuron numbers continuously decrease after treatment of MTZ at 6 hpt and 12 hpt, and are completely gone at 1 dpt. **(B)** Quantification of YFP+ neurons at time points indicated in YFP+ control (red line) and YFP+ MTZ groups (blue line). The YFP+ control group maintains stable cell numbers

across all time points. In the YFP+ MTZ-treated group YFP+ neuron numbers rapidly decline at 6 hpt, with near-complete ablation by 1 dpt. **(A-C)** Maximum projection confocal images of dissected intestines at time point indicated. Data presented as mean (n = 10 larvae per group, 2 experiments); hpt = hours post-treatment, dpt = hours/days post-treatment; Scale bar = 100 μm.

868

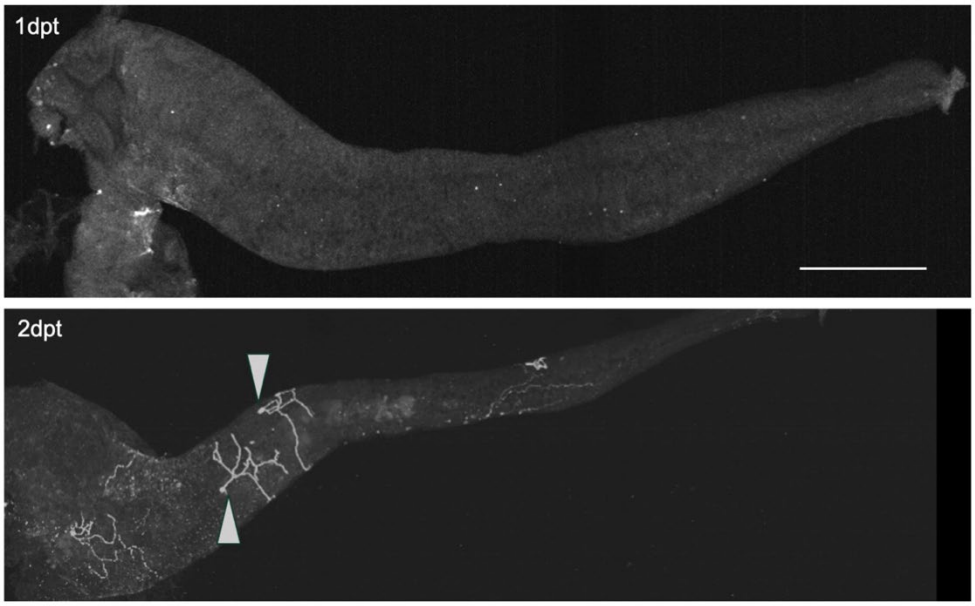

Figure S3. Regenerating neurites in YFP+ neurons following ablation. At 2 dpt, newly generated YFP+ neurons form neurites as the beginning step of neuron regeneration. Upper panel: at 1 dpt there is complete ablation of YFP+ neurons. Lower panel: at 2 dpt developing neurites that form a bridge (arrow) between the newly generated neurons (n = 6 larvae per group. 2 experiments). Maximum projection of confocal image of dissected intestine at time point indicated. dpt = days post treatment; Scale bar = 100 μm.

869

870

871

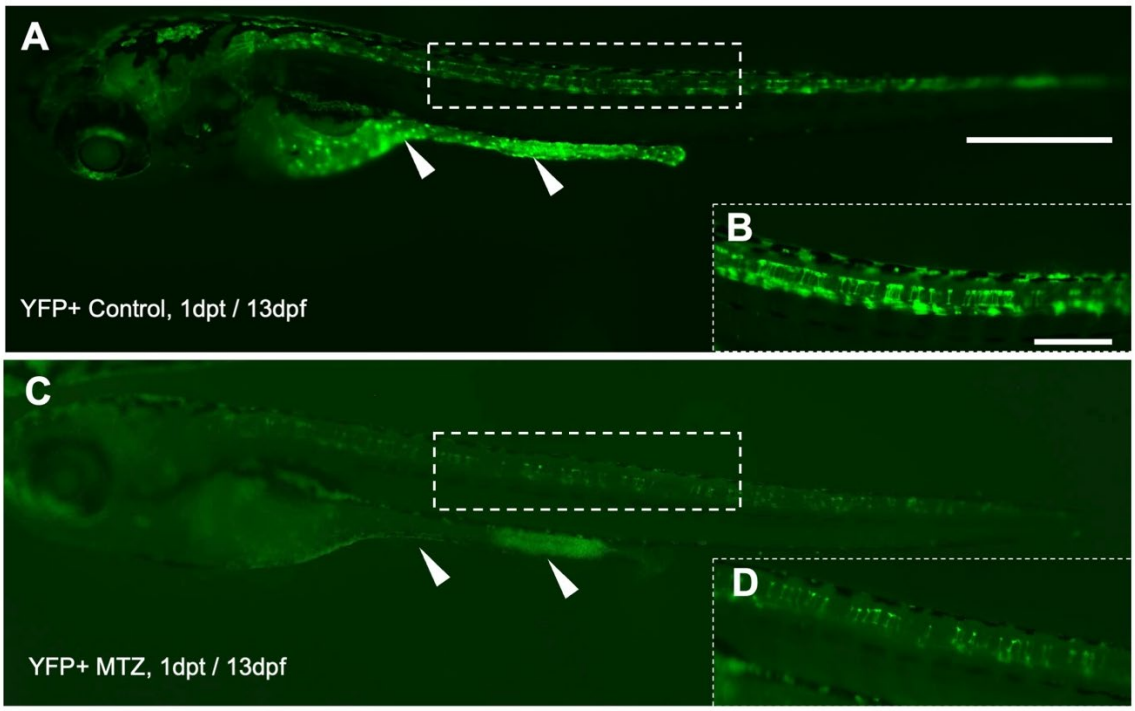

Figure S4. Off-target ablation of YFP+ cells from the spinal cord region. (A) In YFP+ control larvae, the intestine contains a network of YFP+ ENS neurons along the gut and in cells within the area of the spinal cord and in the brain. **(B)** Magnified view shows YFP+ cells in the spinal cord area. **(C)** In YFP+ MTZ treated larvae, YFP+ ENS neurons are essentially absent. **(D)** Magnified view shows that YFP+ cells in spinal cord area are also reduced after MTZ treatment, demonstrating off-target NTR-mediated cell ablation in the spinal cord. (**A-C)** Whole-mount side views of live images of YFP+ control (untreated) and YFP+ MTZ (treated) at stages indicated**.** Arrowheads indicate reporter-positive cells in the gut region. Dashed box outlines the region for magnified view. dpt = days post treatments; (A, C) scale bar = 100 μm; (B, D) scale bar = 20 μm.

872

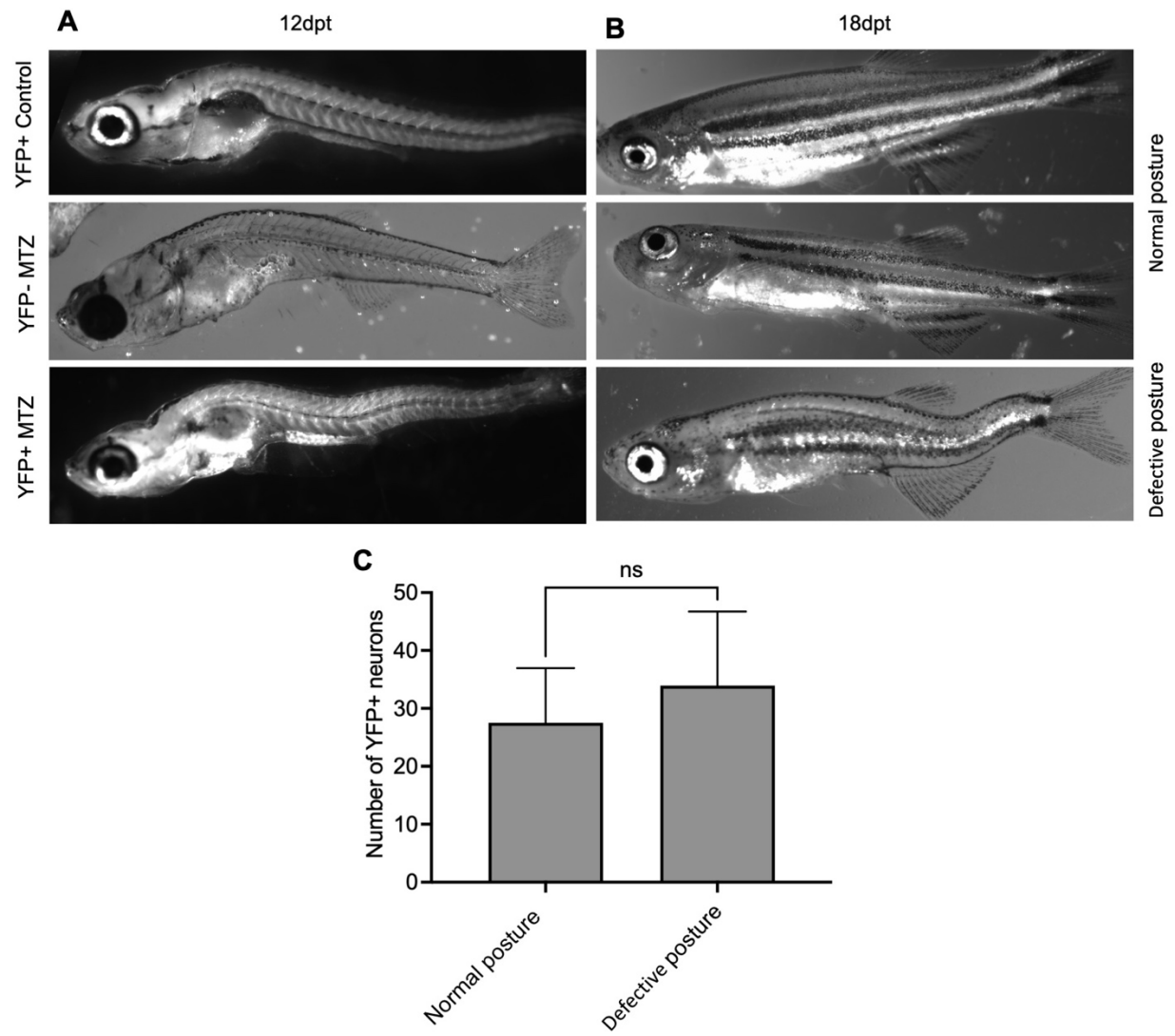

Figure S5. Abnormalities in body posture do not affect YFP+ neuron regeneration. (A-B) Whole-mount side views of larvae at stage indicated from treated (YFP-/+ MTZ treated) and Control (YFP+ untreated) groups. Only half of YFP+MTZ treated shows the body posture defect after 9 dpt. **(C)** The bar graph shows the number of regenerated YFP+ neurons in normally developed larvae compared to those with defective body posture at 12 days post treatment. Data presented as mean ± SD (n = 8 larvae per group, 2 experiments); ns = no statistically significant differences; Scale bar = 100 μm.

873

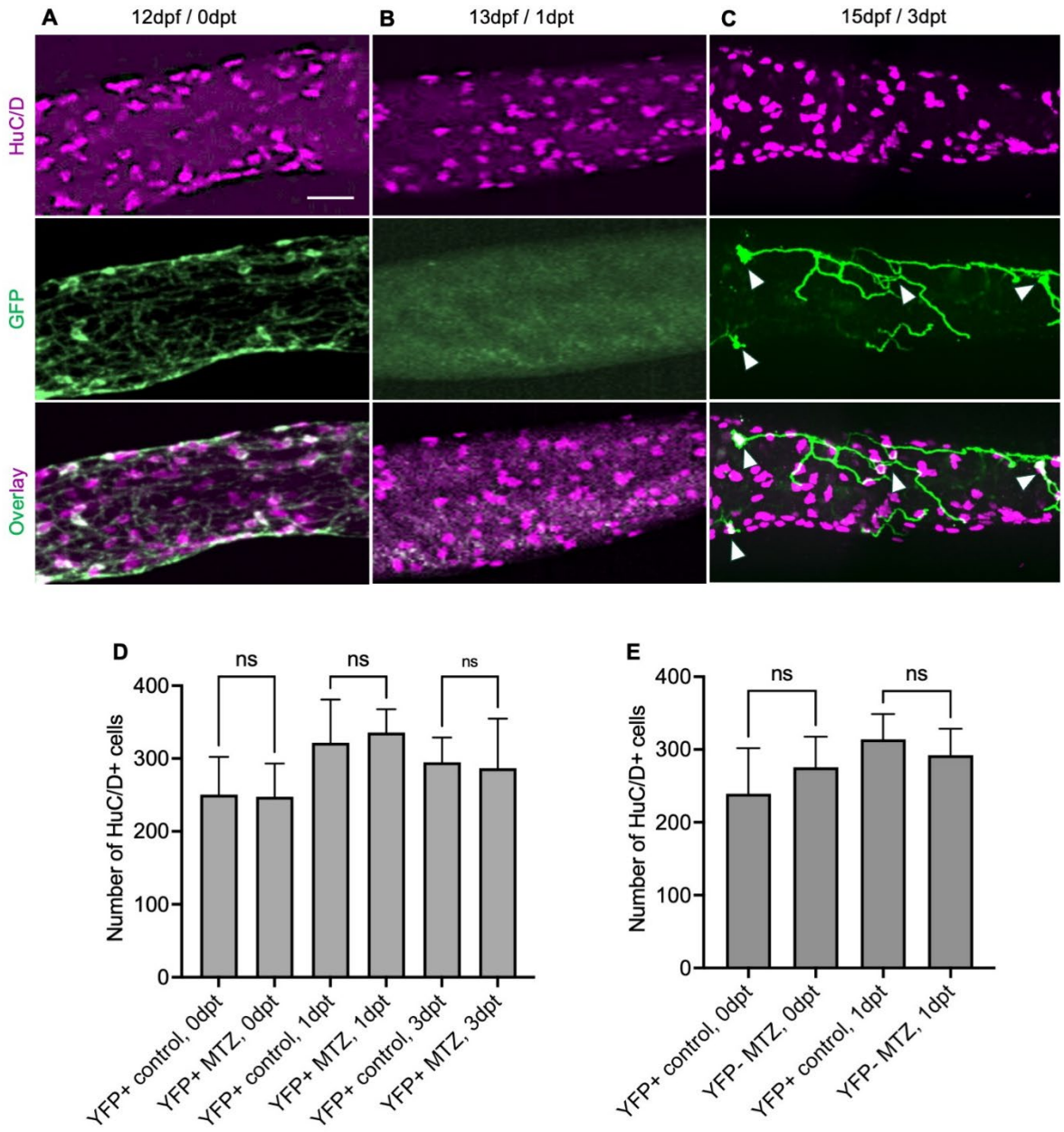

Figure S6. YFP+ neuron loss and MTZ treatment of YFP- larvae does not affect neuron numbers. (A) At 12 dpf (before treatment, 0 dpt), the pan-neuronal marker HuC/D (magenta) and YFP+ cells (labeled with anti-GFP, green) show high colocalization (overlay). **(B)** Following MTZ treatment at 13dpf (1dpt), GFP-HuC/D+ cells are present, whereas GFP+ cells are completely absent due to ablation of YFP+ neurons. **(C)** 15dpf (3dpt) shows GFP+ cells and exons (indicated by while arrow) regeneration process. **(D)** Quantification of HuC/D-positive neuron counts before (0 dpt) and after MTZ treatment (1 and 3dpt). There was no significant difference in total HuC/D+ cells between control and treatment group (n = 10 larvae

per group, 2 experiments). **(E)** Quantification of HuC/D+ neurons in the gut in YFP- MTZ treated and YFP+ untreated controls at 12dpf (before MTZ treatment) and 13dpf (after MTZ treatment). Bar graph shows the number of HuC/D+ cells. No significant difference was observed between treatment groups (n = 10 larvae, 2 experiments). Data presented as mean ± standard deviation; ns = not significant, dpt = days post treatment. **(A-C)** Maximum projection confocal images of dissected intestines. Scale bar = 100 µm; Data are presented as mean ± SD, ns = not significant; dpf = days post fertilization; dpt = days post treatment.

874

875

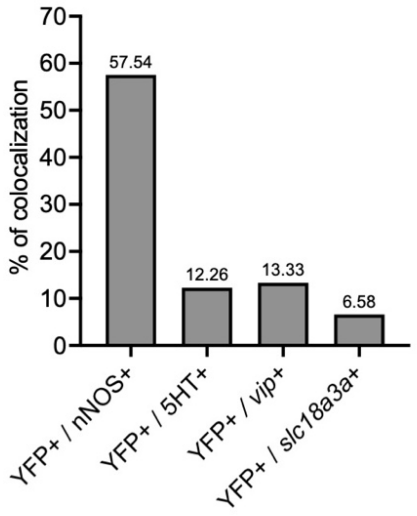

Figure S7. The YFP+ neuronal population consists of different neuronal subtypes at 12 days post fertilization. Quantification of YFP and neuronal subtype colocalization. Bar graph shows the percentage of co-expression of each subtype marker with YFP at 12 days post fertilization / 0 day post treatment. Data presented as mean (n = 10 larvae per group, 2 experiments).

876

877

878 **Supplementary videos have been uploaded to the designated repository.**

Groups	Video description
1dpt	Video S1 = YFP- MTZ Video S2 = YFP+ control Video S3 = YFP+ MTZ
3dpt	Video S4 = YFP- MTZ

	Video S5 = YFP+ control Video S6 = YFP+ MTZ
9dpt	Video S7 = YFP- MTZ Video S8 = YFP+ control Video S9 = YFP+ MTZ
dpt = days post treatment	

879